NTNU

Norwegian University of
Science and Technology

Development of Composite Cathodes for Solid Oxide Fuel Cells

Maria Angeltveit

Materials Technology
Submission date: June 2017
Supervisor: Kjell Wiik, IMA
Co-supervisor: Guttorm Syvertsen-Wiig, CerPoTech AS
Sophie Labonnote-Weber, CerPoTech AS

Norwegian University of Science and Technology
Department of Materials Science and Engineering

Preface

This master's thesis, and the work presented in this report, has been carried out at the Department of Materials Science and Engineering at the Norwegian University of Science and Technology (NTNU), the spring of 2017. The project is a part of the Master program Industrial Chemistry and Biotechnology, specializing in Materials Chemistry and Energy Technology. My main supervisor has been Professor Kjell Wiik, and my co-supervisors have been Guttorm Syvertsen-Wiig and Sophie Labonnote-Weber at CerPoTech AS.

The work has been a continuation of the project work, conducted the fall of 2016, *Development of next generation cathodes for solid oxide fuel cells*.

Maria Angeltveit
Trondheim, June 2017

Acknowledgements

I would like to thank my supervisor, Professor Kjell Wiik, for guidance and help throughout the semester, and my co-supervisors Guttorm Syvertsen-Wiig and Sophie Labonnote-Weber at CerPoTech AS for answering questions and taking part in planning the project. All three for letting me work on the field of solid oxide fuel cells and for letting me contribute with research in the important field of energy technology. I have gained invaluable knowledge and experience throughout my final year at NTNU thanks to you.

Further, I would like to thank Laura Rioja-Monllor and Dr. Carlos Bernuy-Lopez. Laura Rioja-Monllor for guidance in the practical work when producing samples and conducting impedance measurements, and Dr. Carlos Bernuy-Lopez for guidance with impedance measurements and help with analyzing my results, both for sharing their experience within the field and willingness to help me when I needed it. All the members of the Inorganic Materials and Ceramics Research Group should also be thanked for the good feedback at the weekly group meetings, creating a good working environment for the master students. Trond Brandvik deserves a special thanks for valuable discussions and input, and being there for me this past year. I would also like to thank the technical staff at the Department of Materials Science and Engineering for giving me training on the different instruments used.

Lastly, I would like to thank my class at Chemical Engineering and Biotechnology. These past five years would not have been the same without you.

Abstract

Solid oxide fuel cells have the potential to become an important device for clean energy production. Today, these cells run at high temperatures, which cause degradation in the cell components and a short lifetime for the device. To increase the lifetime so that the fuel cell can become economically beneficial, the operating temperature needs to be reduced. For this, new materials that give a low area specific resistance (ASR) at low temperatures need to be developed. Two composite materials have been investigated for cathode performance, both consisting of 70 % $Ce_{0.9}Gd_{0.1}O_{2-\delta}$ and 30 % $La_{0.6}Sr_{0.4}Co_{0.2}Fe_{0.8}O_{3-\delta}$. Composite A was directly spray-pyrolysed by CerPoTech AS, consisting of a well-dispersed mixture of the two materials and thus a high density of reaction cites for the oxygen reduction reaction to occur. Composite B was mechanically mixed using pure LSCF and CGO, also delivered by CerPoTech AS. Dense CGO pellets were produced, and composite cathode was deposited using an air-brush technique. Each sample was heat treated at 650-1150 °C with a 100 °C interval. SEM analysis of the cross sections was conducted to evaluate the adhesion of cathode to electrolyte. Further, symmetric cells with Composite A and Composite B cathode, heat treated at 950 °C and 1050 °C, were tested for cathode performance at 600 °C, 700 °C and 800 °C in dry air atmosphere. The area specific resistance (ASR) at each operating temperature and the activation energy for the four samples were calculated. Composite A had a lower ASR for all operating temperatures and for both heat treatment temperatures. The difference in ASR between the two composites, heat treated at 950 °C, was significant, Composite A a having an ASR comparable to literature values. The activation energy was closer to the activation energy for the oxygen surface exchange reaction, suggesting that this was the dominating rate-limiting process in the cathode. Comparing to pure LSCF cathode, found in literature, Composite A heat treated at 950 °C had a significantly lower ASR at operating temperature 600 °C and a low activation energy. The results for Composite A was attributed to the synthesis method, giving fine grained material with a high density of triple phase boundaries. The lower ASR at 600 °C compared to pure LSCF was believed to be due to a high ionic conductivity of CGO at lower temperatures. A spray-pyrolysed composite cathode is a promising material for

the use in solid oxide fuel cells, due to a low ASR at low operating temperatures, and low activation energy.

Sammendrag

Okside brenselceller har et potensiale til å bli viktige enheter for produksjon av energi. I dag kjøres cellene ved høy temperatur, noe som forårsaker degradering i komponentene og en kort levetid for cellen. For å forbedre dette må driftstemperaturen i brenselcellen senkes, slik at levetiden øker. Dette kan oppnås ved å produsere nye materialer som har en lav arealeffektiv motstand ved lavere driftstemperatur. To kompositttmaterialer har blitt undersøkt for katodeytelse, begge bestående av 70 % $Ce_{0,9}Gd_{0,1}O_{2-\delta}$ og 30 % $La_{0,6}Sr_{0,4}Co_{0,2}Fe_{0,8}O_{3-\delta}$. Kompositt A var direkte spray-pyrolysert, og bestod av en godt dispergert blanding av de to materialene og en høy tetthet av trippelpunkter, mens kompositt B var en mekanisk blanding av de to materialene. Alle materialer ble levert av CerPoTech AS. CGO pelleter ble produsert, og kompositt materiale ble deponert med en "air-brush". Hver prøve ble varmebehandlet ved 650-1150 °C, med et intervall på 100 °C. SEM-analyse ble utført av tverrsnittet av prøvene for å undersøke vedheft av katode på elektrolytten. Symmetriske celler med Kompositt A og Kompositt B ble produsert og varmebehandlet ved 950 °C og 1050 °C. Disse ble testet ved 600 °C, 700 °C og 800 °C i tørr luft. Den arealspesifikke motstanden ved hver kjøretemperatur og aktiveringsenergi for alle prøvene ble beregnet. Kompositt A hadde en lavere arealspesifikk motstand ved alle kjøretemperaturene sammenlignet med Kompositt B. Ved varmebehandling på 950 °C var forskjellen mellom de to kompositten stor, og Kompositt A hadde en arealspesifikk motstand ved 600 °C som var sammenlignbar med litteratur. Sammenlignet med LSCF katoder, funnet i litteraturen, hadde Kompositt A varmebehandlet vet 950 °C en mye lavere arealspesifikk motstand ved 600 °C og en lav aktiveringsenergi. De gode resultatene for den spray-pyrolyserte kompositten skyldes det høye overflatearealet og en større konsentrasjon av trippelpunkter i materialet, og er et bra alternativ for katodemateriale i brenselceller.

Contents

Chapter 1

Introduction

1.1 Background

The world's energy consumption is increasing for each day that passes on. Today, the energy supply sector is the largest contributor to global green house gas emissions. Using fossil fuels as its main source of energy [2], it contributes to the increase in the CO_2-concentration in the atmosphere, which has never been this high. The increase in CO_2-concentration in the atmosphere causes the Earth's average temperature to rise, which again leads to melting of the world's ice sheets, the sea levels to rise and more extreme weather [3]. In November 2016, the Paris Agreement, an international climate agreement working on limiting the temperature rise to less than 1.5 °C took effect [4]. To meet the demanding energy requirement and at the same time stop the temperature from increasing, the outlet of CO_2 need to be reduced and the production of «green» energy needs to be improved.

The solid oxide fuel cell (SOFC) is one of the most promising candidates for «green» energy production, utilizing the chemical energy of renewable sources for production of electrical power. The device has an advantage of fuel flexibility, allowing it to run at several types of fuels such as hydrogen, hydrocarbons and carbon [5], and has a high efficiency compared to other solutions for renewable energy production [6]. The SOFC, in particular, has a high efficiency compared to other fuel cell systems. Even though the SOFC will produce carbon dioxide when running at biomass-derived fuels, this outlet is balanced by previous CO_2-adsorption in plant

matter [6].

The SOFC will be an important device for commercial production of clean energy. The technology is well developed, but still needs some improvements for the fuel cell to be economically beneficent [6]. Today, yttria stabilized zirconia-based SOFCs are available and used in Japan for heating and electricity production [7], but the high operating temperature should be lowered to reduce material degradation and enhance the lifetime of the cell. To achieve this, devices with new materials that work well at lower operating temperatures, need to be investigated [5].

To lower the operating temperature of the cell, a cathode with both high ionic and electronic conductivity at lower temperatures is needed. The number of triple phase boundaries in the component, where the reduction of oxygen occurs, is of importance, as well as thermo-mechanical compatibility between the components, porosity and mechanical strength. A composite based cathode, consisting of materials exhibiting high ionic conductivity and electronic conductivity at lower temperatures, is believed to perform well at reduced operating temperatures [8, 9].

1.2 Aim of work

The aim of this master's thesis has been to establish a procedure for producing a symmetric cell, and testing its performance. Two different composite materials were investigated, both with the composition of 70 % $Ce_{0.9}Gd_{0.1}O_{2-\delta}$ (CGO) and 30 % $La_{0.6}Sr_{0.4}Co_{0.2}Fe_{0.8}O_{3-\delta}$ (LSCF). The main difference between the two materials was the synthesis route. Composite A was directly spray-pyrolyzed, thus consisting of a well-dispersed mixture of the two materials as well as nano-sized particles, while Composite B was mechanically mixed from pure LSCF and CGO.

The first part of this work was to investigate the adhesion and sintering of composite cathode to CGO electrolyte, and establish a procedure for producing symmetric cells. Further on, cells with composite cathodes were produced for testing using impedance spectroscopy at different operating temperatures in dry air atmosphere.

Chapter 2

Literature Review

2.1 The Solid Oxide Fuel Cell

The solid oxide fuel cell converts chemical energy into electrical power. The device run at temperatures above 800 °C, and uses air and fuels such as hydrogen, carbon monoxide and methane. This is the most efficient way of converting stored chemical energy into electricity, reaching an efficiency of 90 % [10]. The SOFC has a fuel flexibility, which allows it to be used in today's hydrocarbon fuel infrastructures [5]. This makes the SOFC a good competitor to other solutions for renewable production of electricity, such as windmills and solar cells. However, before the SOFC can be commercially viable, some improvements to the device have to be made.

The SOFC consist of a dense ionically conducting membrane, with a porous anode at one side and a porous cathode on the other side. An outer circuit connecting the anode and cathode transports electrons back to the cathode, producing electricity [11]. Fig. 2.1 illustrates a solid oxide fuel cell, with the corresponding reactions occurring at the anode and at the cathode.

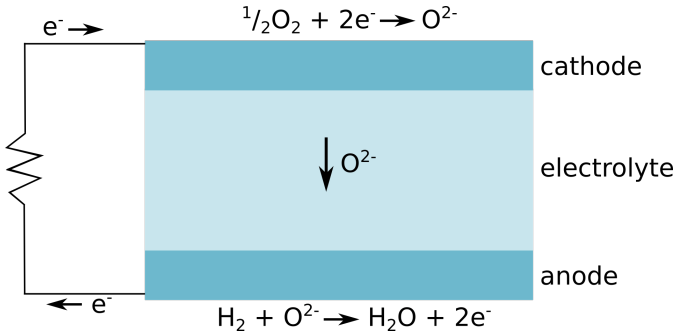

Figure 2.1: Sketch of a solid oxide fuel cell, with the corresponding reactions occurring at the anode and at the cathode. Hydrogen is utilized as fuel for this example.

Oxygen is reduced at the cathode, Eq. 2.1, and the produced oxygen ions move through the dense electrolyte membrane to the anode. At the anode, the oxygen ions react with the fuel, Eq. 2.2, producing water and electrons. The electrons travel back to the cathode through an outer circuit, generating electricity. The reaction occurring at the anode side depends on what fuel is used, here represented by hydrogen.

$$\frac{1}{2}\mathrm{O_2(g)} + 2\mathrm{e^-(cathode)} \rightarrow \mathrm{O^{2-}(electrolyte)} \tag{2.1}$$

$$\mathrm{O^{2-}(electrolyte)} + \mathrm{H_2} \rightarrow \mathrm{H_2O(g)} + \mathrm{e^-(anode)} \tag{2.2}$$

The driving force for oxygen diffusion through the electrolyte membrane is the difference in chemical potential of oxygen at the anode side relative to the cathode. This difference is due to the difference in oxygen partial pressure, which is much lower at the anode relative to the cathode; hence the chemical potential of oxygen is lower at the anode side. The diffusion of oxygen ions is thermally activated, which explains why the cell works better at temperatures above 800 °C [12].

2.1.1 Components of the SOFC

The electrolyte should have a high ionic conductivity and negligible electronic conductivity. To limit ohmic losses across the electrolyte, the membrane should be thin and have a high density. The electrolyte should also have good mechanical properties to withstand thermal stresses as the temperature is cycled from room temperature, when the device is not in use, to high temperatures during operation. The most used electrolyte is currently yttria-stabilized zirconia (YSZ).

Yttrium is a lower valent cation relative to zirconium, and by doping ZrO_2 with Y_2O_3, oxygen vacancies is induced in the lattice to maintain electroneutrality [12]. To obtain a high ionic conductivity, a large number of vacant cites where oxygen ions can move to and from is needed. A high temperature increases the thermal energy of the oxygen ions, which improves the transport of ions between such empty sites [13].

The electrodes, placed on each side of the electrolyte membrane, need to have high electrocatalytic activity and high electronic conductivity to minimize the effective resistance in the cell [14]. The thermal expansion coefficient of the material should match the one of the electrolyte and the current collector. This is because the cells are cycled between room temperature and a high operating temperature, leading to expansion and contraction of the materials. The materials also need to be chemically stable and have a stable microstructure at higher temperatures [14].

The anode acts as an electrocatalyst, where the oxide ions from the electrolyte oxidize the fuel. The produced electrons from this process are transported towards the current collector and into the external circuit. The choice of anode material depends on electrolyte and the type of fuel used in the cell [14]. Nickel-YSZ is the most widely used anode material. This is a composite-based anode where nickel act as a catalyst for fuel oxidation and YSZ is ionically conducting, transporting the oxygen ions from the electrolyte to the reaction cite [14].

The cathode act as a catalyst for the oxygen reduction reaction, according to Eq. 2.1. The reaction takes place at triple-phase boundaries (TPB) where the gas, the cathode material and electrolyte material intersect. Electrons need to be transported from the outer circuit to the reaction cite, and oxygen ions need to be transported away from the reaction cite to the electrolyte membrane.

2.1.2 Promising materials for use in SOFC

CGO

In more recent studies, $Ce_{0.9}Gd_{0.1}O_{2-\delta}$ (CGO) has shown to be a promising electrolyte material for intermediate temperature SOFCs [8]. CGO has a high ionic conductivity at intermediate temperatures compared to YSZ-based electrolytes

and is stable at operating conditions [15]. Studies show that a composition with 10 mol % gadolinium gives the highest value for ionic conductivity [12]. A drawback for CGO is that in reducing conditions at temperatures above 600 °C, Ce^{4+} is reduced to Ce^{3+} [12]. Reduction of cerium induces n-type semi conduction in the material, causing an increase in the unit cell volume, which again can cause reduction in the mechanical strength and crack formation in the component [14]. Considering that the aim is to reduce the operating temperature for the SOFC, reaching for 600 °C and lower, this should not be a problem. CGO is compatible with cobalt containing perovskite oxides as cathode when considering the thermal expansion coefficient [14].

The fluorite structure of CGO consists of a cubic close packing of cations with anions in tetrahedral holes [13], illustrated in Fig. 2.2.

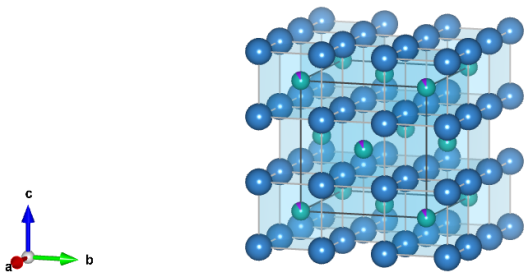

Figure 2.2: Fluorite crystal structure of CGO, where blue anions are oxygen, green cations are cerium and purple cations are gadolinium. The figure was generated in VESTA software [16].

Doping with a lower valent cation, Gd^{3+}, induces formation of oxygen vacancies to maintain electroneutrality in the lattice. These oxygen vacancies make the material a good ionic conductor [17]. The Kröger-Vink notation for doping with Gd^{3+} is seen in Eq. 2.3.

$$Gd_2O_3 \xrightarrow{CeO_2} 2\,Gd_{Ce}{}' + V_O{}^{\bullet\bullet} + 3\,O_O{}^{X} \tag{2.3}$$

LSCF

$La_{0.6}Sr_{0.4}Co_{0.2}Fe_{0.8}O_{3-\delta}$ (LSCF) is a good cathode material, having both good electronic and ionic conductivity at 800 °C [14, 18]. At lower temperatures, the ionic conductivity is drastically reduced due to the high activation enthalpy of oxygen self-diffusion [19]. LSCF has a perovskite crystal structure, illustrated in Fig. 2.3. In the ideal case, the system is cubic and consists of close-packed AO_3-layers with B occupying all the interlayer octahedral holes. A is a large cation, B is a small cation and by substitution of one of these, or both, the catalytic activity, ionic and electronic conductivity of the material can be tailored [20].

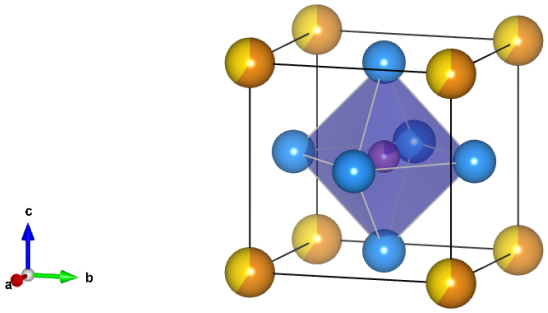

Figure 2.3: The perovskite crystal structure of LSCF. Orange and yellow A-site cations are lanthanum and strontium, respectively. Pink and purple B-site cations are iron and cobalt, respectively. Oxygen anions are blue, located at the faces of the unit cell. The figure was generated in VESTA software [16].

In a non-ideal case, the perovskite crystal structure can vary between different non-cubic structures. Based on the size of the cations in the crystal structure, the Goldschmidt tolerance factor t, expressed in Eq. 2.4, gives an indication of what distortions the perovskite undergoes.

$$t = \frac{\sqrt{2} r_{\text{A-O}}}{2 r_{\text{B-O}}} \tag{2.4}$$

where $r_{\text{A-O}}$ is the bond length between A-cation and oxygen and $r_{\text{B-O}}$ is the bond length between B-cation and oxygen. Deviation from unity indicates more energy in the structure, and for $t \leq 0.75$ or $t \geq 1.06$, the structure will change to lower or higher symmetries, respectively [21]. $La_{1-x}Sr_xCo_{0.2}Fe_{0.8}O_{3-\delta}$ has been reported to have a rhombohedral unit cell at room temperature for $x \geq 0.3$ [22], while $La_{0.8}Sr_{0.2}Co_{1-y}Fe_yO_{3-\delta}$ has an orthorombic unit cell for $y \geq 0.8$ [23].

In LSCF, having a combination of La^{3+} and Sr^{2+} induces oxygen vacancies in the material. This substitution also leads to mixed valence of cobalt, introducing holes in the valence band and increasing the electronic conductivity of the material. A high electronic conductivity enhances the catalytic activity of the material due to reduction in the polarization resistance associated with the charge transfer process when oxygen gas is reduced to oxygen ions [24]. $La_{1-x}Sr_xCoO_{3-\delta}$ (LSC) has an unusually high thermal expansion coefficient, compared to other SOFC electrolytes. Substitution of Co^{3+} with Fe^{2+} reduces the thermal expansion coefficient (TEC), giving a TEC closer to the CGO electrolyte. This is without compromising the electrochemical performance of the material [25, 26].

The Kröger-Vink notation of charge compensation in LSCF can be seen in Eq. 2.5 and Eq. 2.6.

$$SrMO_3 \xrightarrow{LaMO_3} Sr_{La'} + M_M{}^{\bullet} + 3\,O_O{}^{X} \tag{2.5}$$

$$2\,M_M{}^{\bullet} + O_O{}^{X} \rightarrow 2\,M_M{}^{X} + V_O{}^{\bullet\bullet} + \frac{1}{2}O_2(g) \tag{2.6}$$

Eq. 2.5 represents the mixed valence mechanism, which is the oxidation of a B-site cation to a higher valent cation. Eq. 2.6 represents the oxygen vacancies in the lattice. The condition of electroneutrality in the material is expressed in Eq. 2.7

$$[Sr_{La'}] = [M_M^{\bullet}] + 2[V_O^{\bullet\bullet}] \tag{2.7}$$

Three charge carriers are present in LSCF; electrons, holes and oxygen vacancies. Temperature and oxygen partial pressure affect what carriers are dominating, hence to what extent Eq. 2.5 and Eq. 2.6 takes place. Holes are the main charge carriers over electrons due to a higher concentration of holes over the total range of oxygen partial pressure measured [27]. At low oxygen partial pressure, oxygen vacancies are dominating, while at higher oxygen partial pressure, electron holes are important [27]. Ionic and electronic conductivity as a function of oxygen partial pressure is illustrated in Fig. 2.4 [27].

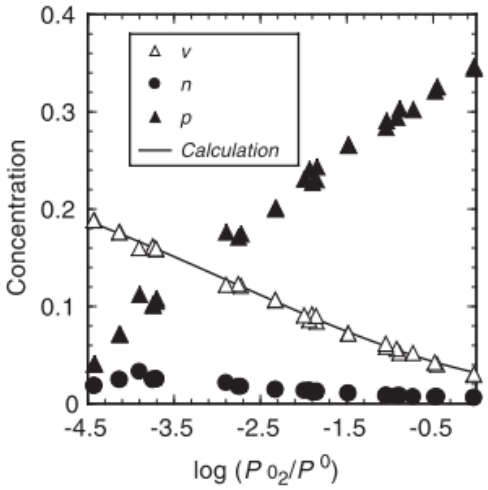

Figure 2.4: Ionic and electronic conductivity domains in $La_{0.6}Sr_{0.4}Co_{0.8}Fe_{0.2}O_{3-\delta}$ as a function of oxygen partial pressure at 800 °C. p, n and v represents holes, electrons and oxygen vacancies, respectively. The figure is reprinted from [27].

The electronic conductivity in LSCF has been found to be dependent of both temperature and amount of La-substitution [22]; it increases as temperature is increased, reaching a maximum, then decreasing. The conductivity below this temperature is attributed to the adiabatic polaron hopping mechanism and is expressed in Eq. 2.8 [22]. Polaron hopping is the hopping of an electron hole between two valence states [26]. The temperature at maximum electronic conductivity decreases with increasing Sr-content [22].

$$\sigma = \frac{A}{kT} e^{\frac{-E_a}{kT}} \tag{2.8}$$

where A is the material constant, k is the Boltzmann constant, T is the temperature, and E_a is the activation energy. Available sites for polaron hopping occurs when mixed valence of the B-cation creates charge compensation [22]. The activation energy associated with this is reduced and the electrical conductivity is increased due to more mobile charge carriers [22]. Since both the pre-exponential term and the exponential term is dependent on temperature, the conductivity will reach a maximum at a certain temperature. This maximum will correspond to T = $\frac{E_a}{k}$, but it is assumed that other mechanisms will dominate the conductivity as the temperature is increased [22]. By evaluating the charge carrier concentration of polaron hopping, one can obtain information about the other mechanisms. The charge carrier concentration is expressed in Eq. 2.9, in terms of the fraction of available hopping sites occupied by charge carriers.

$$C = (1 + e^{(\frac{Qe}{k})})^{-1} \tag{2.9}$$

C is the site occupancy, Q is the Seebeck coefficient and e is the elementary charge. This is documented to be dependent on both temperature and Sr-content [22]. The site occupancy is increased as the temperature is increased, and can be explained by the mechanism of charge disproportionation of Co^{3+}, where two Co^{3+} ions go to Co^{2+} + Co^{4+} [22]. This is thermally activated, hence the charge carrier concentration increase as the temperature is increased. On the other hand, the reduction in site occupancy at higher temperatures can be due to oxygen vacancies. This was observed to increase as the temperature was increased [22], which is important for the ionic conductivity in LSCF. The oxygen vacancies at high temperatures can explain the reduction in electrical conductivity, seen in Fig. 2.5.

2.2 The oxygen reduction reaction

The mechanisms and kinetics of the oxygen reduction reaction (ORR) are still not well understood. The reaction occurs in several steps, depending on the type of cathode material it is occurring on. First, oxygen molecules are adsorbed on the solid surface and become partly reduced ionic species. Further, the oxygen ions are transported to the electrolyte across the surface, along the interface or through the bulk of the cathode material [29]. It is shown that the kinetics of the ORR can be governed by both charge transfer and diffusion, as adsorption of oxygen molecules and diffusion of oxygen ions to the triple phase boundaries could be

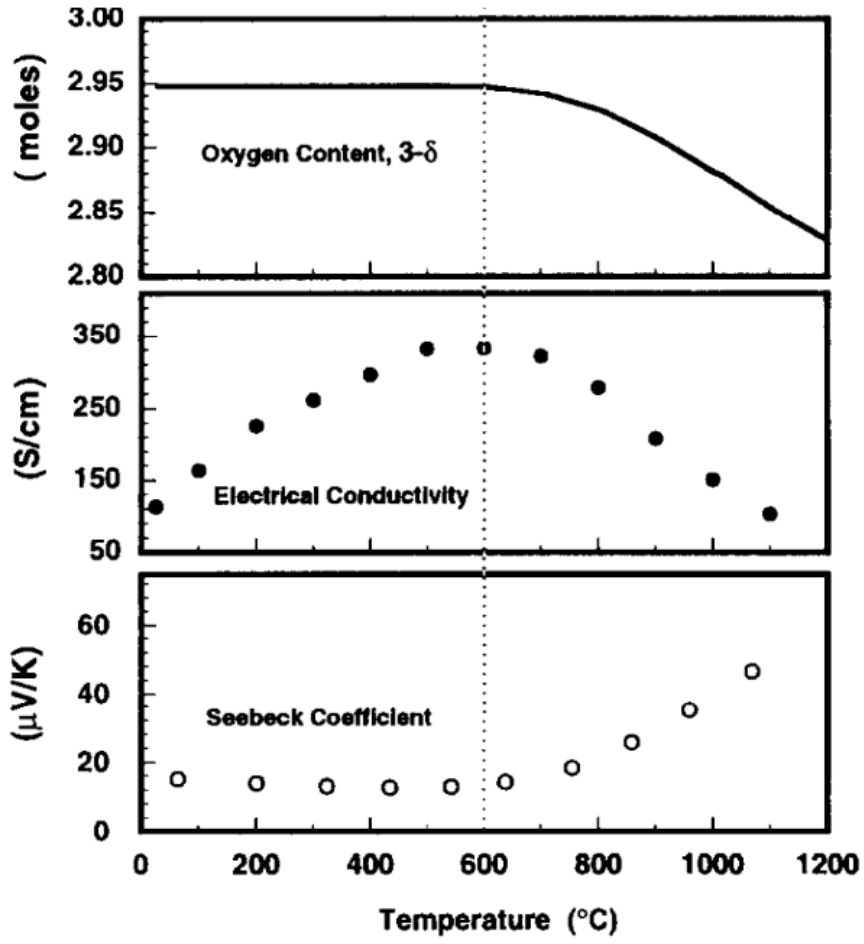

Figure 2.5: Oxygen content, electrical conductivity and the Seebeck coefficient in $La_{0.6}Sr_{0.4}Co_{0.2}Fe_{0.8}O_{O-\delta}$ as a function of temperature. Reprinted from [28].

interconnected [30]. When considering a mixed ionic electronic conducting (MIEC) cathode, the mechanisms become even more complicated, since the MIEC allows for transport of oxygen through the bulk material [31].

2.3 Cathode design

The cathode in a solid oxide fuel cell can be divided in three main categories; (a) a porous single-phase electronic conductor, (b) a porous two-phase composite of electronically and ionically conducting materials and (c) a porous single-phase mixed ionic and electronic conducting material [29]. A sketch of these three can be seen in Fig. 2.6. The limiting factor controlling the performance of a cathode in a SOFC is the operating temperature. The temperature dependency of the ionic conductivity in a MIEC material will lead to poor performance of the cathode at lower temperatures.

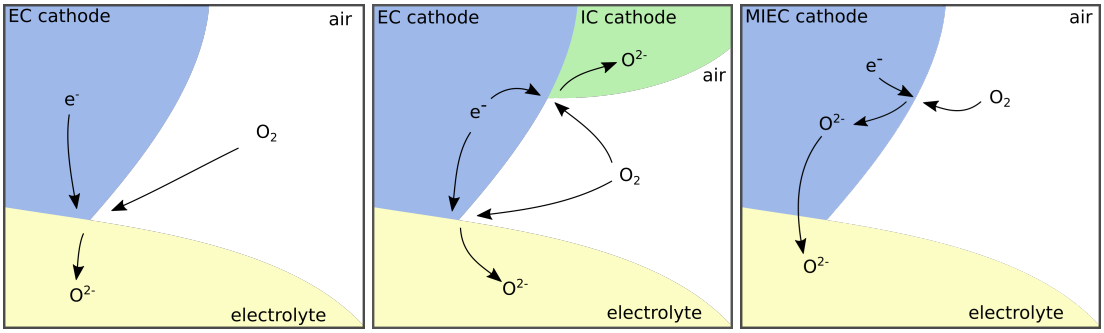

Figure 2.6: Sketches of the three main types of cathodes described in [29]. (a) a single-phase electronic conductor, (b) a two-phase composite cathode of ionic and electronic conducting material and (c) a single-phase mixed ionic electronic conducting material. EC, IC and MIEC stands for electronic, ionic and mixed ionic and electronic conducting, respectively.

By producing a composite based cathode consisting of both a MIEC material, in this case LSCF, and a material which has a good ionic conductivity at lower temperatures, in this case CGO, the total performance of the cathode at intermediate temperatures will be enhanced. A high density of TPB will contribute to the reduction of the area specific resistance (ASR) as well. A sketch can be seen in Fig. 2.7. A second benefit of using an electrolyte consisting of pure CGO together with a composite based cathode with CGO, is that the thermal expansion mismatch

between the two components will be strongly reduced, depending on the amount of CGO in the cathode [19].

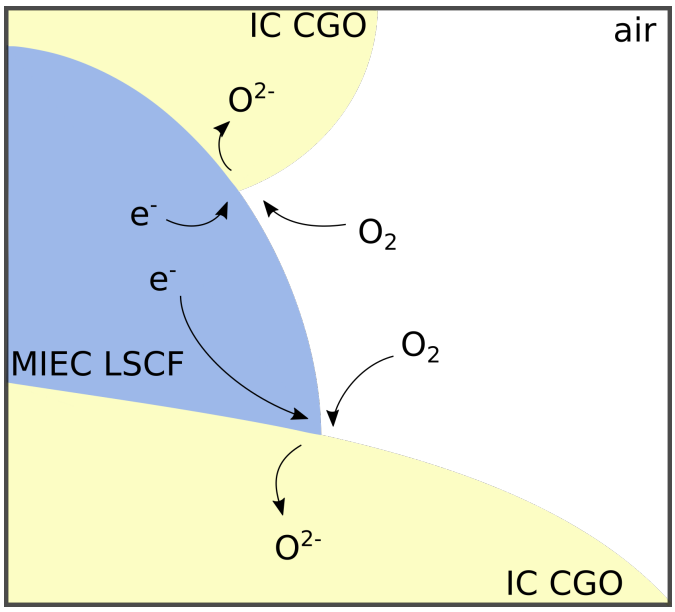

Figure 2.7: Sketch of a composite cathode consisting of the ionically conducting material CGO and the mixed ionically electronic conducting material LSCF. The reduction of O_2 is occurring at the triple phase boundaries.

2.3.1 Nanostructured materials

The electrochemical performance of a SOFC is highly dependent on the material choice and also the microstructure of the electrodes [32]. Nanostructured electrodes have been considered to improve the performance of the cathode due to the high surface area to volume ratio. By producing a composite based cathode with nanostructured materials, a high number for TPB is obtained together with a large surface area of the materials. This is illustrated in Fig. 2.8. Nanostructured materials are produced using spray-pyrolysis, a versatile and economically beneficial technique, giving a good control of the grain size and morphology of the material by adjusting the process parameters [15].

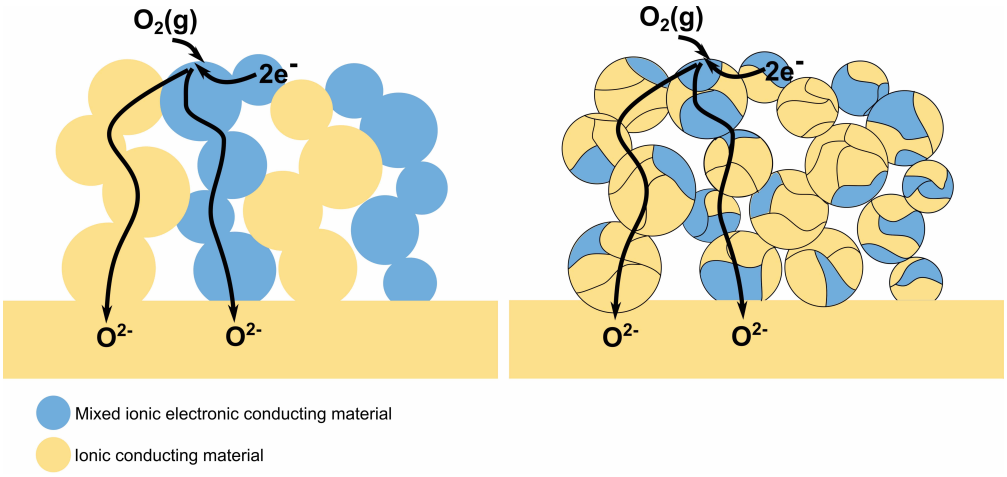

Figure 2.8: Sketch of a mechanically mixed composite cathode and a spray pyrolysed composite cathode, both consisting of a mixed ionic electronic conducting material, and an ionically conducting material. The bottom part is the ionically conducting electrolyte.

Shimada et al. [33] produced nanostructured composite cathode powder consisting of $La_{0.6}Sr_{0.4}MnO_{3-\delta}$ (LSM) and YSZ by spray-pyrolysis. The cathode was sintered at 1200 °C, and the individual particles had a small size of 100-200 nm. Spray-pyrolysis gave a well dispersed composite cathode with an intimate mixture of the two materials. Illustrating this, STEM-images was recorded of La and Zr, and can be seen in Fig. 2.9. The images show that the each grain of LSM and YSZ are completely separated, and connected to each other creating its own network structures. It was also reported that Mn and Sr was overlapping with La, and Y overlapped with Zr. This lead to a three-dimensional extension of the electrochemically active region [33]. Further, the narrow particle size distribution gave rise to uniform pore channels, and together with the microstructure of the composite cathode, this provided a high concentration of TPB [33].

In a composite based cathode, consisting of a high density of triple phase boundaries, the mixture needs to be well dispersed, the grains in the starting material need to be small in size and exaggerated grain growth should be avoided during heat treatment. High performance in composite based cathodes is found to be due to a fine grained microstructure and a high porosity of the cathode. A good porosity enhances gas transport in the cathode [19]. It is found that the threshold thickness of the cathode is 10 to 15 times the size of the particles in the ionically conducting phase in the cathode. The smaller particles, the thinner layer is needed for minimal polarization resistance [34].

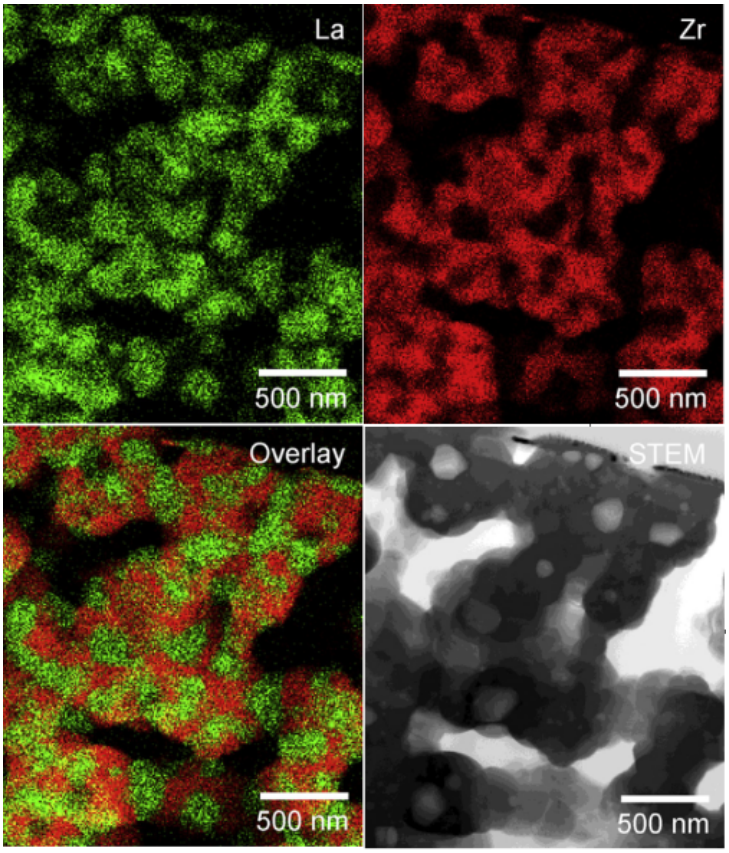

Figure 2.9: Microstructure of a composite cathode consisting of LaSrMgO and ZrYO. Mapping of La and Zr, an overlay of the two mappings and a STEM-recording of the same area. The image was reprinted from [33].

A mechanism for material transport activated and driven by a source of energy is needed for grain growth in a material to occur. Heat is the primary source of energy, as well as energy gradients due to contact between particles and surface tension. Small particles provide a high driving force for densification due to a large radius of curvature, which gives more rapid sintering at lower temperatures, but can also lead to agglomeration, grain coarsening and exaggerated grain growth during heat treatment [35].

Production of ceramic materials through spray-pyrolysis gives fine crystallite sized grains of high purity [35–37]. Heat treatment of such material can lead to rapid densification and grain growth, and the material loses surface area. By avoiding grain growth during production, the density of triple phase boundaries will be

high and the area specific resistance in the cell will be reduced.

2.3.2 Grain boundary resistance

A composite material, consisting of one mixed ionic electronic conducting material and one ionically conducting material is a good solution for composite cathodes when considering the mismatch of thermal expansion coefficients in a SOFC. However, the performance of such a composite cathode is not necessarily controlled by the properties of the two individual materials. Interactions between these phases and altered interfaces such as grain boundaries may have an important role in the overall performance of the device. Structural disorder, solute segregation, oxygen vacancy depletion and formation of precipitates are believed to dominate the overall conductivity [38].

Lin et al. [38] investigated the grain boundaries of CGO grains in CGO/$CoFe_2O_4$ (CGO/CFO) composites, and compared the obtained results to single-phase CGO. The measurements can be seen in Fig. 2.10, and show a difference in the Ce^{4+}/Ce^{3+}-, Gd/O- and O/Ce-ratios near CGO-CGO grain boundary in the single-phase CGO. The figure demonstrates the accumulation of Gd-ions at the grain boundary, and formation of a space charge layer reflected by the Ce^{4+}/Ce^{3+}-ratio. In the composite material consisting of CGO and CFO, the Ce^{4+}/Ce^{3+}, Gd/O and O/Ce ratios near CGO-CGO grain boundary showed to be similar to the values in the CGO grain interior. This is illustrated in Fig. 2.10. These results confirm that oxygen vacancy concentration at CGO-CFO grain boundary core in the composite is similar to the concentration of oxygen vacancy in the CGO grain interior. This is explained by the formation of a Gd- and Fe-rich GdFeCoCeO-phase, avoiding the accumulation of Gd-ions and the following oxygen vacancy depletion at the grain boundaries.

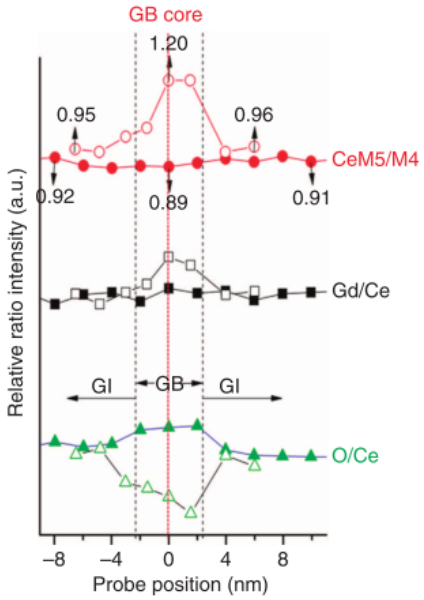

Figure 2.10: Profile of $Ce^{4+}Ce^{3+}$, Gd/O- and O/Ce- ratio near CGO-CGO grain boundary. The solid symbols are measured in a composite material consisting of CGO and CFO, while hollow symbols are from a single-phase CGO. The dotted, red line indicate the grain boundary core between two grains, the area between the two black, dotted lines is the grain boundary and GI indicates the grain interior [38].

In a CGO-based composite cathode, the ionic-electronic transport would be more complex compared to pure CGO due to the possible emergence of new phases with additional grain boundary interfaces. The structure, composition and charge distribution in the grain boundaries may also change during fabrication of a two-phase composite cathode. Additional phases may form due to cation migration at elevated temperatures, which can either promote or obstruct ionic-electronic transport [38]. It is found that CGO and LSCF do not react to form secondary phases when heat treated at 1300 °C [28], suggesting that no phase segregation will occur at the grain boundaries.

Also, the diffusion of cations between electrolyte and cathode is an important feature. Li et al. [39] investigated the interfacial region between LSCF and CGO and found that all cations in both materials diffuse into each other, and that elements in LSCF diffuse into the CGO phase along grain boundaries in the vicinity of the cathode/electrolyte interface, and segregate at grain boundaries and TPBs.

2.4 Characterization of SOFC performance

2.4.1 Impedance spectroscopy

Impedance spectroscopy (IS) is carried out to evaluate the electrochemical behavior of electrode and electrolyte materials, and the degradation mechanisms occurring, in a SOFC [40]. Usually the measurements are done on a pellet shaped symmetrical cell consisting of two identical electrodes on each side of an electrolyte membrane. The standard way of measuring the impedance is to apply a known single-frequency voltage to the symmetric cell and measuring the current response at that frequency [40].

The impedance is given by the ratio between the applied voltage, *V(ω)* and the current response, *I(ω)*, seen in Eq. 2.10 [15].

$$Z(\omega) = \frac{V(\omega)}{I(\omega)} = \frac{V_0 e^{-i\omega t}}{I_0 e^{-i(\omega t+\phi)}} = \frac{V_0}{I_0} e^{i\phi} \tag{2.10}$$

The impedance function is expressed in Eq. 2.11 through the Euler-relation [15].

$$Z(\omega) = Z_{\text{real}}(\omega) + iZ_{\text{imag}}(\omega) \tag{2.11}$$

where ω is the angular frequency and i is the imaginary number. The real component of Eq. 2.11 is also called the resistive component, and the imaginary component of Eq. 2.11 is also called the capacitive component. A resistance and a capacitance in parallel characterize different regions of a ceramic symmetric cell sample. The characteristic time constant, τ, of each parallel RC-element is given by the product of R and C, seen in Eq. 2.12. Eq. 2.13 shows the relation between ω_{max}, the resistance and the capacitance, which makes R and C separable. This makes it possible to separate the different RC elements and assign them to different regions in the sample [41].

$$\tau = RC \tag{2.12}$$

$$\omega_{\text{max}} RC = 1 \tag{2.13}$$

2.4.2 Area specific resistance

The area specific resistance (ASR) in a SOFC is the resistance in the electrode corresponding to 1 cm^2 of the cell. A low ASR implies fast kinetics, while a high ASR implies slow kinetics in the cathode. There are three ways of reducing the internal resistance of the cell; use electrodes with high conductivity, a good design of the cell and making the electrolyte as thin as possible. This is difficult due to the need of mechanical strength [42].

The impedance measurements are represented in a Nyquist-plot, where the negative imaginary part is plotted along the y-axis and the real part is plotted along the x-axis. The resulting graphs represent rate-limiting electrode processes occurring in the sample. The charge transfer resistance is seen as the diameter of the semicircle. From *f(max)*, the double layer capacity C_{dl} can be calculated [15]. The area specific resistance (ASR) is found as half the charge transfer resistance, illustrated in Fig. 2.11 [41].

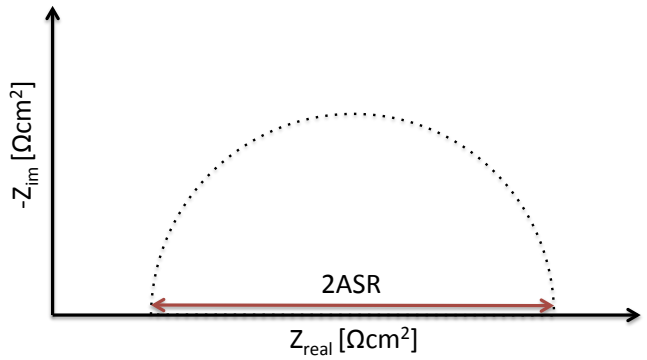

Figure 2.11: Sketch of a Nyquist-plot, showing the relationship between the semi-circle and the area specific resistance in the electrode.

To evaluate the resulting Nyquist-plot, equivalent model circuits are used. This approximates the measured impedance over the range of frequencies measured using circuit elements such as resistors, inductors and capacitors. The impedance behavior of an electrochemical interface reaction can be described by a parallel combination of a resistor and a capacitor, sketched in Fig. 2.12. R represents the ohmic resistance of the electrolyte and the lead wires in the set-up, R_1 models the kinetics of the electrochemical reaction, while the capacitor reflects the capacitance of the interface [41].

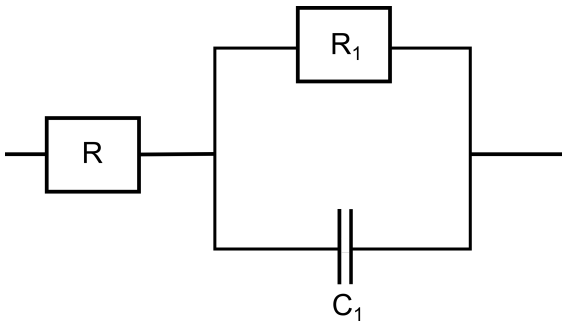

Figure 2.12: Model of an equivalent circuit, used to approximate the measured impedance as a parallel combination of a resistor and a capacitor, connected in series with a resistor. R represents the ohmic resistance of the electrolyte and the lead wires, R_1 represents the kinetics of the electrochemical reaction and C_1 represents the capacitance of the interface [41].

Several processes take place in the cell when it is electrically stimulated; transport of electrons through the electronic conductors, transfer of electrons at the electrode-electrolyte interface and the flow of charged atoms via defects in the material. Ideally, impedance spectroscopy is able to de-convolute all the separate processes taking place.

The impedance response of symmetric cells with mixed ionic electronic conducting cathodes can consist of three distinct resistances. i) Is the ohmic resistance of the electrolyte. ii) Is the charge transfer resistances at interfaces, including electronic transfer at the interconnect/-electrode interface and ionic transfer at the electrode/electrolyte interface. iii) Is the chemical impedance of non-charge-transfer processes, including oxygen surface exchange, solid-state and gas-phase diffusion. An example of a Nyquist-plot is seen in Fig. 2.13. High frequency, medium frequency and low frequency semi-circles corresponds to electron transfer, ionic transfer and chemical diffusion resistance, respectively [43].

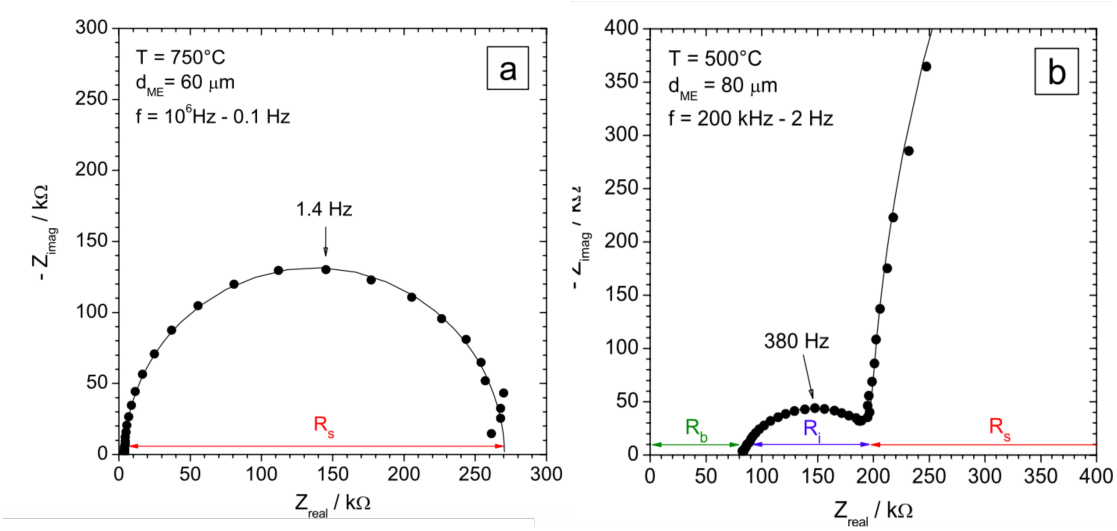

Figure 2.13: Example of Nyquist-plots obtained from samples tested at two different temperatures. At high temperatures (a), only the low frequency resistance is visible. At lower temperature (b), the medium frequency resistance is visible and the high frequency arc intercept [43].

2.5 Previous work [1]

Two composite materials consisting of 70 % CGO and 30 % LSCF were characterized with respect to phase purity, crystallite- and grain size, and sintering kinetics, all as a function of heat treatment temperature. Composite A was directly spray-pyrolyzed and delivered as-produced, while Composite B was mechanically mixed using pure components. The two composites were wet-milled and heat treated at 600 °C, 700 °C and 800 °C, and further characterized as a function as heat treatment.

Grain size and sintering kinetics

Nitrogen adsorption was conducted, estimating the grain size as a function of heat treatment temperature. Composite B consisted of smaller grains when heat treated at 600 °C, 700 °C and 800 °C compared to Composite A, seen in Fig. 2.14. The reason for the larger grain size for Composite A was assumed to be due to the smaller particle size prior to heat treatment, which came from the production method. Smaller grains induce grain growth at lower temperatures. Composite B consisted of larger particles prior to heat treatment.

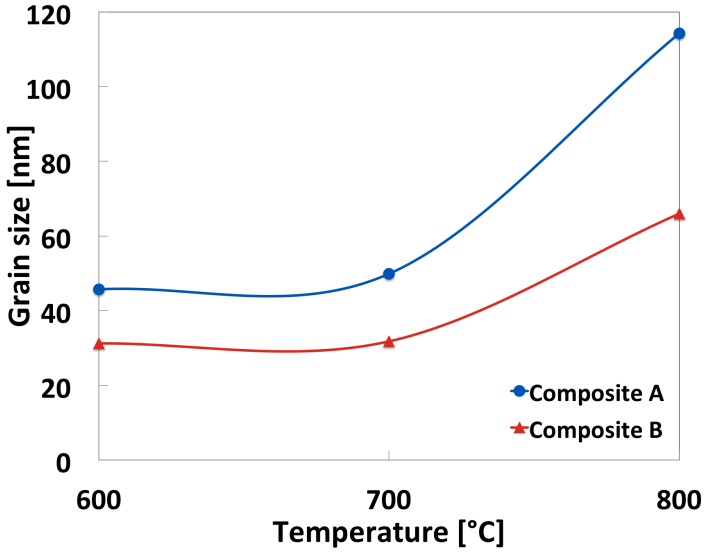

Figure 2.14: The grain size of Composite A and Composite B as a function of heat treatment temperature. The grain size is calculated from the specific surface area, obtained from nitrogen adsorption measurements [1].

The sintering kinetics of the two composites was investigated using dilatometry.

The results showed that Composite A started to densify at around 650 °C, while Composite B started to densify at around 800 °C. The results of the dilatometry can be seen in Fig. 2.15. This corresponded well with the calculated grain size. Since Composite A started to densify at lower temperatures, and also then experiences coarsening at even lower temperatures, the nitrogen adsorption measurements showed larger grains in Composite A at temperatures above 600 °C.

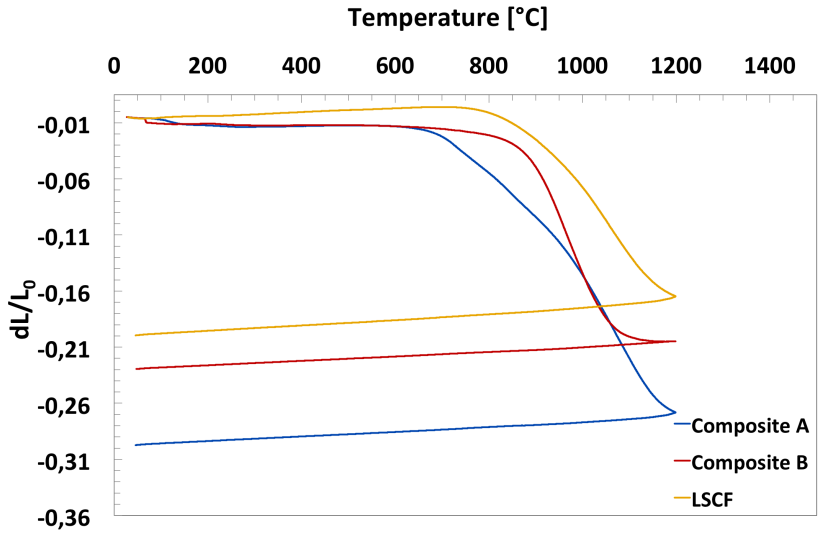

Figure 2.15: Dilatometry of Composite A, Composite B and LSCF. The program was set to 1200 °C with a heating and cooling rate of 10 °C/min, and was conducted in synthetic air.

Phase purity and crystallite size

The crystallite size of the two composites was calculated using Topas Software [44], showing that Composite A consisted of smaller crystallites compared to Composite B at 600 °C and 700 °C. In both composites, the crystallites grew drastically between 700 °C and 800 °C. LSCF and CGO in Composite B showed a larger difference in crystallite size compared to Composite A.

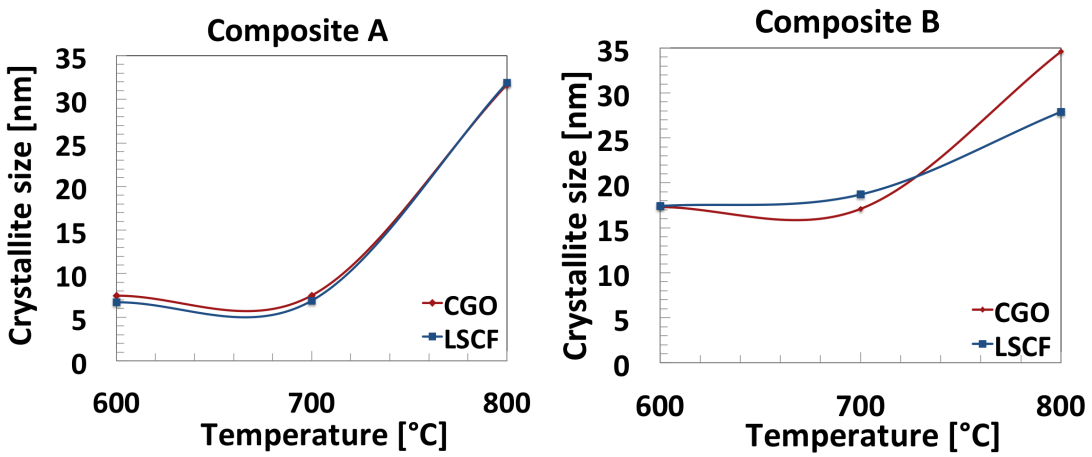

Figure 2.16: Crystallite size for LSCF and CGO in Composite A and Composite B as a function of heat treatment temperature. Calculations are done in Topas software [44].

The crystallite size of Composite A was smaller than for Composite B at 600 °C and 700 °C, and both materials experienced a significant crystallite growth between 700 °C and 800 °C. The same was seen when investigating grain growth, except Composite B consisted of smaller grains at all temperatures compared to Composite A. Composite A had a lower sintering temperature, which is explained by Composite A being directly spray-pyrolyzed while Composite B was mechanically mixed. Both composites were treated at 650 °C to avoid any grain growth before further production of symmetric cells.

Chapter 3

Experimental work

This chapter describes the experimental procedure and methods conducted in this thesis, allowing the work to be repeated on a later occasion.

3.1 Apparatus and chemicals

Two different composites were synthesized, characterized and heat treated during previous work [1]. Sample name, composition and method of production is presented in Tab. 3.1.

Table 3.1: Ceramic powder synthesized by spray-pyrolysis and delivered by CerPoTech AS. LSCF = $La_{0.6}Sr_{0.4}Co_{0.2}Fe_{0.8}O_{3-\delta}$ and CGO = $Ce_{0.9}Gd_{0.1}O_{2-\delta}$

Sample	Composition	Comment
Composite A	30 % LSCF + 70 % CGO	Produced from a homogeneous water based solution, directly spray-pyrolysed. Heat treated at 650 °C.
Composite B	30 % LSCF + 70 % CGO	CGO and LSCF synthesized separately by spray-pyrolysis, LSCF calcined at 700 °C and milled prior to mechanically mixing with CGO. Heat treated at 650 °C.

The apparatus used during the experimental work are listed in Tab. 3.2, together with model and application of use.

Table 3.2: List of apparatus, with model and application, used in the experimental work.

Apparatus	**Model**	**Application**
Ball mill	U.S. Stoneware	Milling and mixing of powders
Furnace	Nabertherm P330	Calcination of powder
Clean furnace	Nabertherm P330	Sintering of pellets
Uniaxial press	Hydraulic C-press	Pressing of pellets
XRD	Bruker D8 Advance DaVinci	Investigation of phases and phase purity
Dilatometer	Netzsch S-3400N	Sintering analysis
Polisher	Struers LaboPol-21	Grinding pellets
Polisher	Struers Tegramin-20	Polishing pellets
Sputter Coater	Cressington 208	Coating samples with carbon for SEM
FE-SEM	Hitachi SU-6600	Investigation of cross section and top surface
Tubular furnace	ProboStat	Setup for impedance measurements
Analyzing system	Alpha-A High Performance Frequency Analyser	Analyzing impedance data

3.2 Symmetric cells - Investigation of heat treatment temperature

3.2.1 CGO electrolyte

CGO powder was delivered by CerPoTech AS already calcined at 600 °C and milled. CGO (100 g.) was grinded in a mortar and sieved with a 250 µm mesh before production of pellets. CGO (0.7 g.) was weighed out for each pellet, and 15 mm diameter pellets were pressed in an uniaxial press with a pressure of 70 MPa for one minute. The pellets were sintered at 1300 °C for 10 hours, with a heating rate of 600 °C/h and a cooling rate of 300 °C/h. The heat treatment program can be seen in Fig. 3.1. The density of the sintered pellets was measured using Archimedes method.

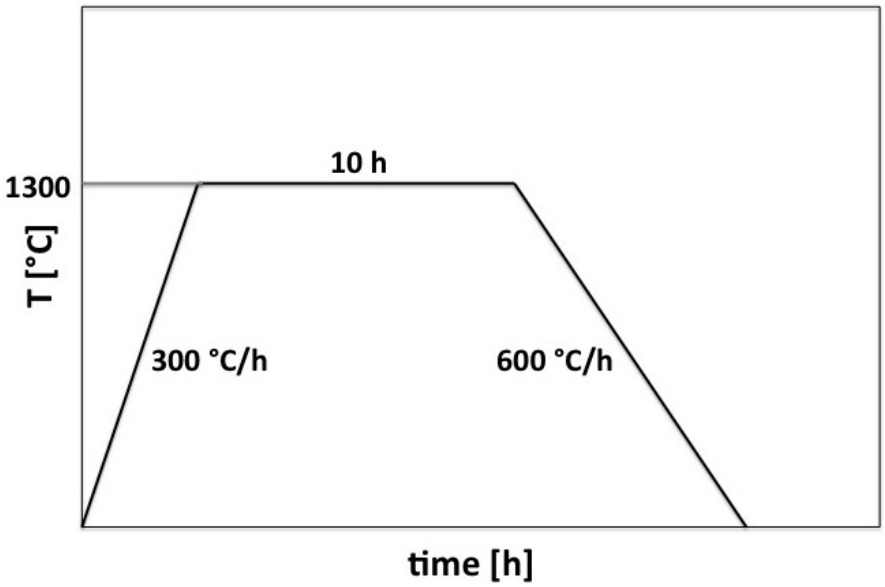

Figure 3.1: Temperature program for sintering CGO pellets in air. The heating rate was set to 600 °C/h, the cooling rate was set to 300 °C/h. 1300 °C/h was held for 10 hours.

The pellets were grinded on one side using a Struers LaboPol-21, starting with grit size P800, then P1000 and ending with P1200 grinding, with 25 µm, 20 µm and 15 µm grain size, respecitvely. A cut across the ungrinded side of the pellets was made. This was to easily cut the pellet in half later on for investigation of the cross section in SEM.

3.2.2 Deposition of composite cathode

Composite A and Composite B were deposited on the grinded side of the pellets using an air-brush. The air-brush was connected to an argon gas outlet with an excess pressure of 0.5 bar. Two solutions were made consisting of 5 wt% composite powder, 3 wt% dolacol and 92 wt% ethanol. The solutions were mixed in an ultra sonic bath for 30 minutes. A strip of tape was attached around the edge of the pellets to avoid deposition of cathode material here. This would give short-circuiting when testing for impedance. The pellets were weighed before and after deposition. In the first session, 5 µg was deposited. This was adjusted to 20 µg for the remaining samples to obtain a thicker cathode layer. A sketch of the samples can be seen in Fig. 3.2.

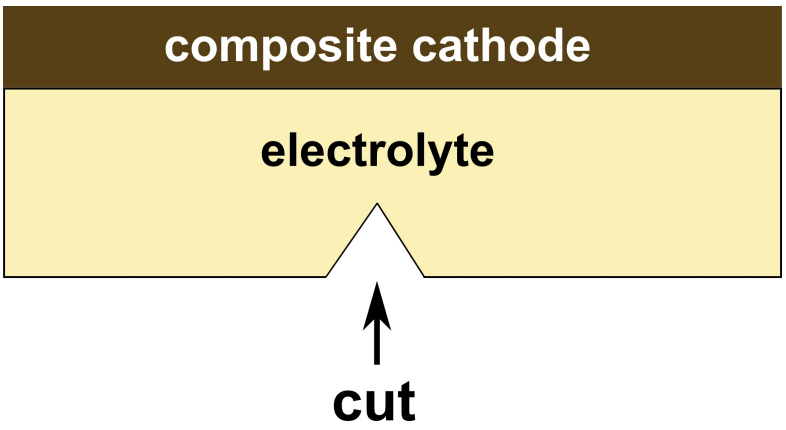

Figure 3.2: Sketch of produced samples for SEM-analysis.

One sample of each composite was heat treated at 650 , 750 , 850, 950, 1050 and 1150 °C. After heat treatment, the pellets were cut in two parts, inducing the crack with a scissor, for investigation of the cross section and top surface in SEM. To investigate how well the composite cathode was adhering to the electrolyte, a swob-test was also conducted by carefully wiping a dry Q-tip across the top surface of the cathode layers.

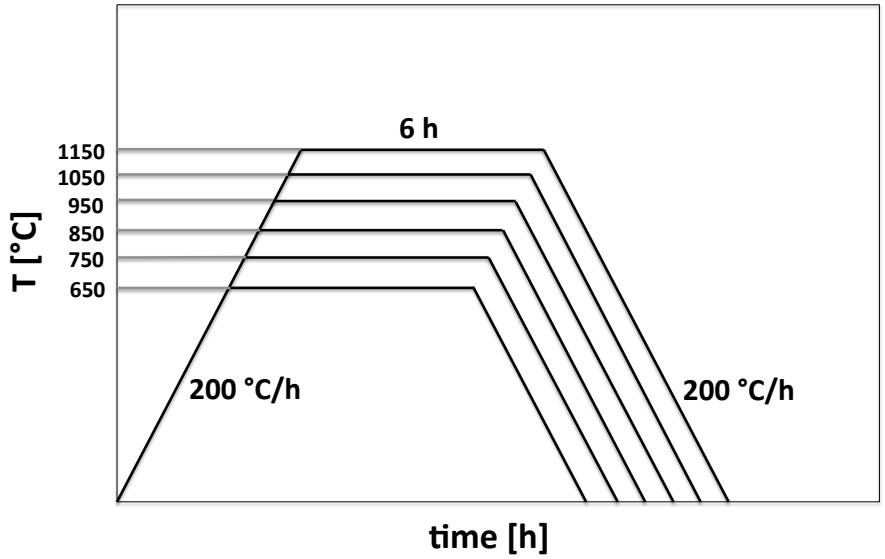

Figure 3.3: Temperature program for heat treatment of CGO electrolyte with deposited composite cathode. The heating and cooling rate was set to 200 °C/h and the temperature was held for 6 hours. The heat treatment was conducted in air.

3.2.3 Scanning electron microscopy

Investigation of the samples, both before and after testing using impedance spectroscopy, was conducted in a Hitachi SU-6600 FE-SEM with an acceleration voltage of 15 kV. For investigation of the cross section, each sample was placed vertically on a sample holder with carbon tape, and coated by using a carbon sputter coater for 10 seconds. For investigation of the top surface, each sample was placed horizontally on a sample holder with a carbon tape, and coated using a carbon sputter coater for 10 seconds.

3.2.4 Energy dispersive spectroscopy

Samples heat treated at 1050 °C and 1150 °C were placed vertically in a casting die and casted in epoxy for element analysis. The casted samples were grinded with SiC paper starting with grit size P500, then P800 and ending with P1200, with 25 µm, 20 µm and 15 µm grain size, respectively, using a Struers LaboPol-21. The samples were further polished using DiaPro Diamond suspension in the following order: Largo, Dur, Mol, with 9 µm, 3 µm and 1 µm grain size, respectively. The samples were cleaned in ethanol in an ultra sonic bath between each polishing step. Before investigation in SEM, the samples were taped with aluminum

tape and coated with carbon using the carbon sputter coater for 10 seconds to avoid charging.

3.2.5 Dilatometry

Dilatometry analysis was performed on pure CGO to measure the change in dimension as a function of temperature, and to calculate the thermal expansion coefficient (TEC). A pellet with dimensions 5 mm diameter, and 2 mm height was pressed using the uniaxial press. The applied pressure was 60 MPa. The measurement was performed in a Netzsch 402C up to 1400 °C in synthetic air, with a heating and cooling rate of 10 °C/min.

3.2.6 X-ray diffraction

The top surface of the two samples chosen for impedance spectroscopy was investigated using X-ray diffraction. This was to calculate the crystallite size of the material in the two cathodes. The samples were placed in single crystal Si sample holders, attached with an adhesive paste. XRD was performed with CuKα radiation of wavelength 1.5406 Å. The scanning was performed from 10 to 75 2Θ angle with scanning time of 30 minutes. The obtained diffractograms were investigated for phase purity using EVA software [45] by comparing with reference PDF 04-002-6160 for CGO and PDF 04-017-2448 for LSCF. The references were found in the International Center for Diffraction Data. Further, the crystallite size of the two materials was calculated using Bruker´s software Topas [44].

3.3 Production of symmetric cells

Dense CGO pellets were prepared following the same procedure described in section 3.1.1. Both sides of the electrolyte pellets were grinded starting with P800, P1000 and finishing with P1200 grinding paper. The pellets were cleaned with 100 % ethanol using a Q-tip, and an air-brush was used for applying composite cathode on each side of the pellet, as described in section 3.1.2. A sketch can be seen in Fig. 3.4. The amount of deposited cathode was adjusted to 40 µg to obtain a thicker cathode layer to achieve better results in the impedance measurements.

The samples tested were heat treated at 950 °C and 1050 °C. These two temperatures were chosen based on investigation of the cross sections done in SEM. Pt-paste was deposited on each side of the pellet, letting the paste dry at 120 °C for 5 minutes in a drying cabinet in between each deposition. An illustration can be seen in Fig. 3.4.

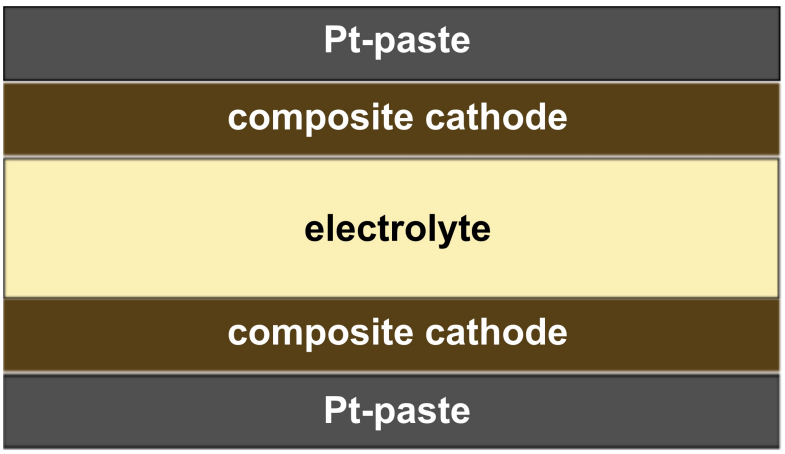

Figure 3.4: Sketch of produced symmetric cells tested for impedance spectroscopy. For these samples, no cut was made across the pellet. This was to more accurately calculate the surface area of both sides of the pellets.

This was done to ensure good contact between the cathodes and the Pt-plates in the sample holders. Due to the noise in the first sample tested, the Pt-pasted was cured at 800 °C for 5 minutes in a furnace for the remaining three samples. The sides of the samples were carefully grinded using a P1200 grinding paper to be sure to avoid short-circuiting, and the diameter of the sample was measured with a digital caliper.

3.4 Impedance spectroscopy

Electrochemical impedance spectroscopy was performed on symmetric cells using a tubular furnace with a ProboStat sample holder setup for circular samples. An Alpha-A High Performance Frequency Analyzer from Novocontrol was used to analyze the impedance response. The measurements were done in dry air atmosphere. The amplitude of the applied AC signal was 50 mV for the first sample. For the following samples, the amplitude was adjusted to 700 mV due to noise in the measurements. The frequency investigated ranged from 1 MHz to 1 mHz.

To investigate the effect of heat treatment temperature, the impedance response was measured at 800 °C, 700 °C and 600 °C. To ensure that no microstructural changes had occurred during testing, measurements were repeated at 800 °C. A sketch of the program can be seen in Fig. 3.5. The samples were let to stabilize for two hours at each temperature before measurement started, and measurements were conducted for three hours at each temperature.

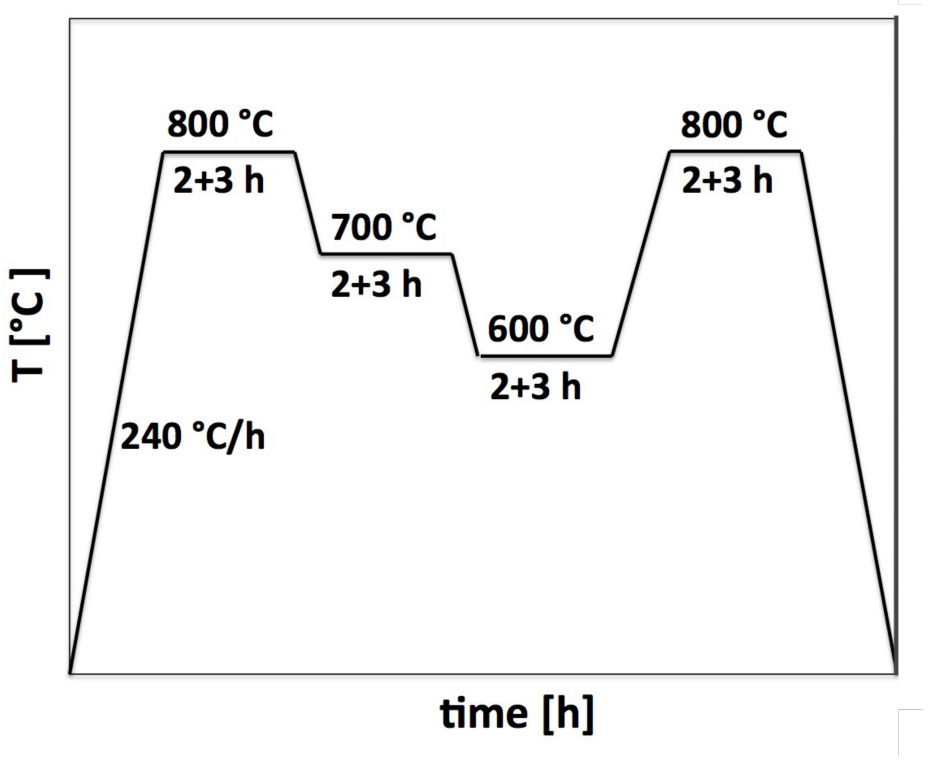

Figure 3.5: Program set for impedance measurements. The measurements were performed at a frequency from 1 MHz to 1 mHz, at amplitude of 50 mV and 700 mV. Each temperature was let to stabilize for 2 hours before measurements were conducted for 3 hours. The heating and cooling rate was set to 240 °C/h.

Processing of the data obtained from the measurements were conducted in ZView software [46].

Chapter 4

Results

In this chapter, abbreviations will be used. A or B indicate what composite is being discussed. These letters will be followed by a heat treatment temperature. E.g. A950 means Composite A heat treated at 950 °C.

4.1 CGO electrolyte pellets

The density of the CGO pellets was measured using Archimedes method, and was found to be above 92 % for all pellets. The grain size was calculated from the obtained SEM-picture, seen in Fig. 4.1, using the linear intercept method. The grains had an average size of 720 nm.

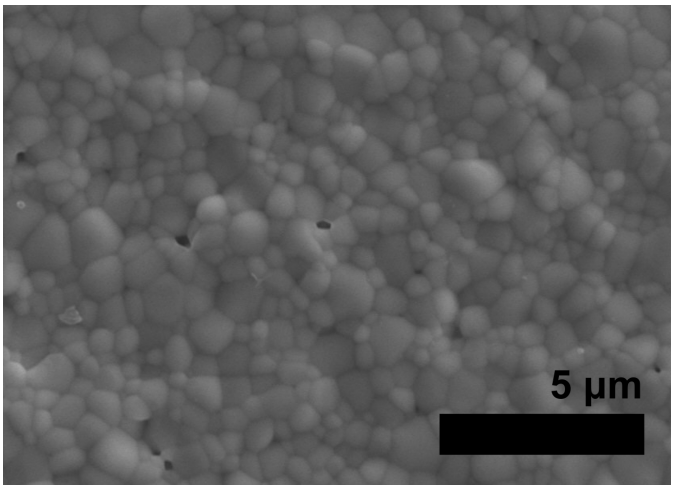

Figure 4.1: Cross section of CGO electrolyte, sintered at 1300 °C for 10 hours.

4.2 Sintering kinetics of CGO

The result from the dilatometer analysis conducted on CGO is presented in Fig. 4.2 . The curve indicates that CGO started to densify at around 600 °C. The TEC was calculated from the dilatometer curve, and found to be $22 \cdot 10^{-6}$ °C^{-1}.

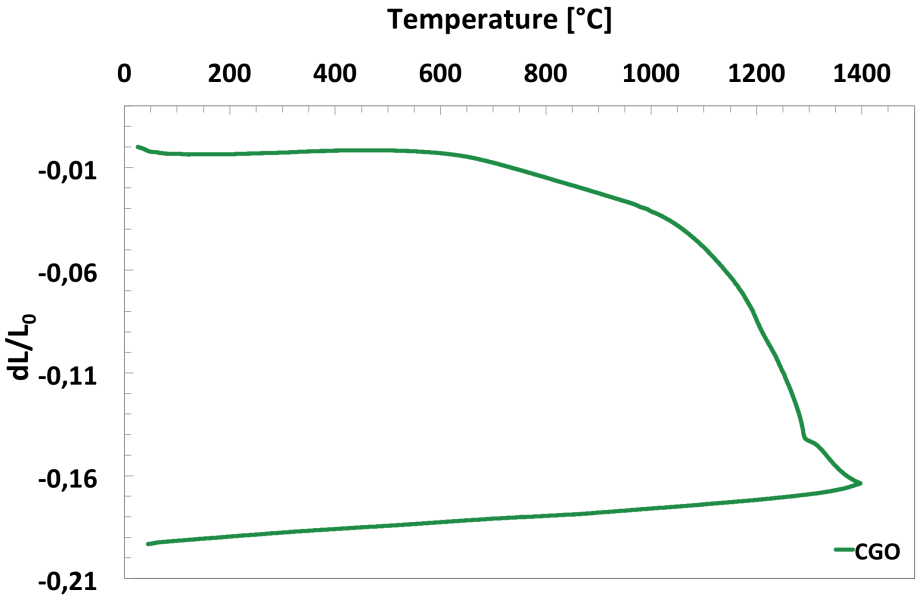

Figure 4.2: Sintering curve for CGO obtained during dilatometer analysis. The temperature was set to 1400 °C, with a heating and cooling rate of 2 °C/min. The analysis was conducted in synthetic air.

4.3 Adhesion of composite cathode

4.3.1 Top surface - Composite A and Composite B

Fig. 4.3 shows the top surface of both Composite A and Composite B, with increasing heat treatment temperature from top to bottom. As the heat treatment temperature for the samples is increased, both composite A and Composite B experience densification and grain growth. Composite A at 750 °C and 850 °C consist of larger particles compared to Composite B at the same temperatures. This is due to coarsening of Composite A during calcination at 650 °C prior to sintering of these samples. This is only occurring in Composite A because it consists of smaller particles due to the synthesis method. This is accounted for in previous work [1]. Composite B is mechanically mixed, and consists of larger grains in the

starting material. This leads to coarsening at even higher temperatures compared to Composite A, and is seen in Fig. 4.3 to be at around 850 °C.

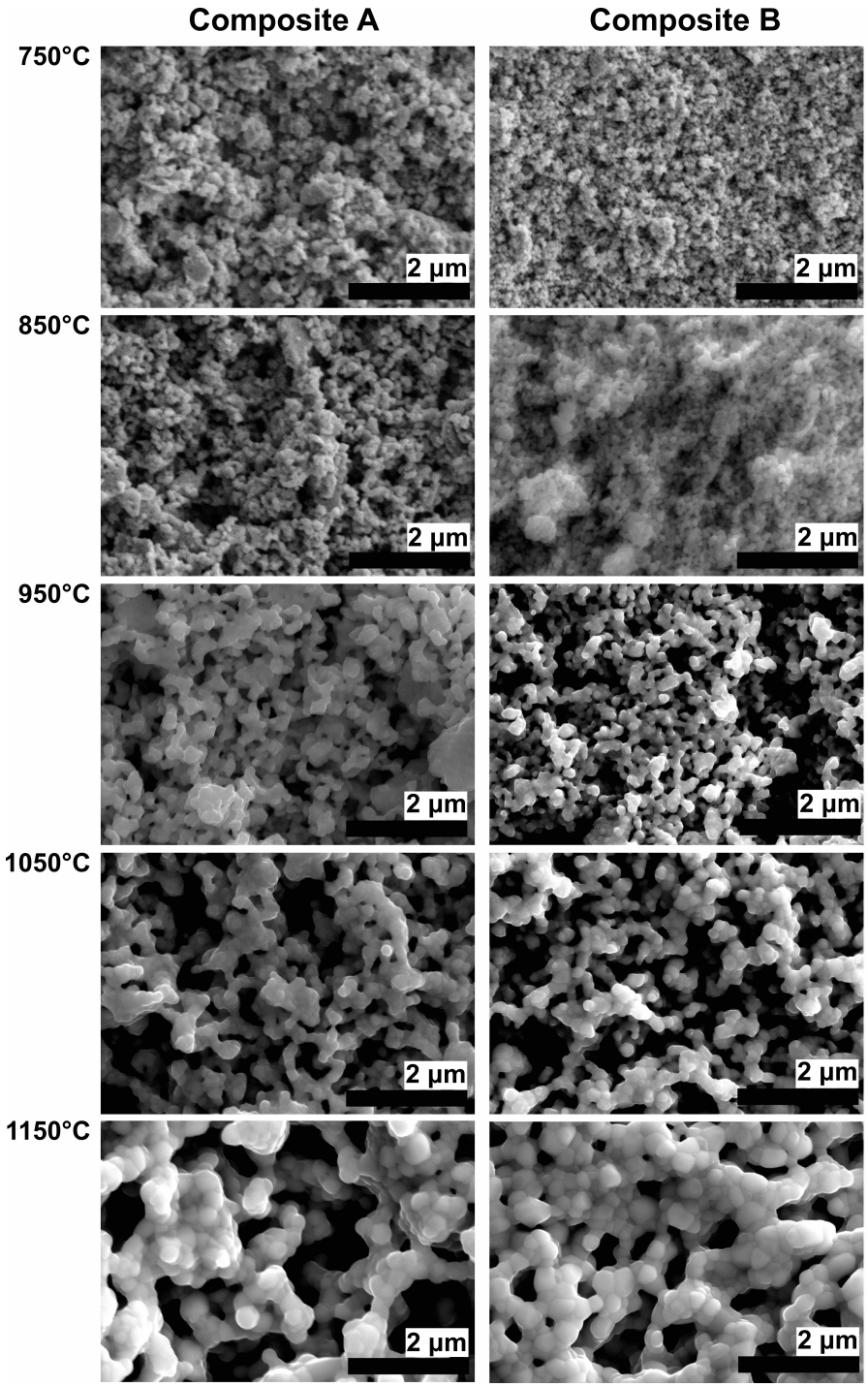

Figure 4.3: SEM images of the top surface of Composite A and Composite B cathode, with increasing heat treatment temperature from top to bottom.

At heat treatment of 1050 °C and 1150 °C, it is evident that grain growth and sintering has occurred, seen by large grains and pores. Densification and grain growth starts between 850 °C and 950 °C for both composites. These results correspond well with the dilatometry measurements seen in Fig. 2.15, and the nitrogen adsorption seen in Fig. 2.14 from previous work [1].

The samples heat treated at 650 °C was not intact after heat treatment, seeing that the cathode material fell of when the samples were further handled. It was decided that these samples were too fragile to investigate further in the research.

The particle size of the heat treated composite cathode material is presented in Tab. 4.1, calculated using the linear intercept method on the SEM-images seen in Fig. 4.3. The ideal thickness for the composite cathode was calculated based on the grain size, and is also presented in Tab. 4.1. Finding the ideal thickness of the cathodes was based on studies reporting that this should be 10 to 15 times the size of the particles in the cathode material [34].

Table 4.1: Particle size calculated from the SEM-recordings seen in Fig. 4.3, and estimated ideal cathode thickness based on the particle size.

Sample	Particle size [nm]	Ideal thickness [µm]	Sample	Particle size [nm]	Ideal thickness [µm]
A750	170	1.7-2.6	**B750**	94	0.9-1.4
A850	180	1.8-2.7	**B850**	120	1.2-1.8
A950	370	3.7-5.6	**B950**	290	2.9-4.4
A1050	450	4.5-6.6	**B1050**	460	4.6-6.9
A1150	450	6.5-6.6	**B1150**	500	5-7.5

4.3.2 Cross section

Composite A

In Fig. 4.4, the cross section of the Composite A cathode heat treated at 850 °C, 950 °C, 1050 °C and 1150 °C is presented. The thickness and density of the cathode layers are presented in Tab. 4.2. The thickness of the cathode layer heat treated at 850 °C is about 1-2 µm thick. The cathodes heat treated at 950 °C, 1050 °C and 1150 °C have a thickness ranging from 8 µm to 5 µm. The thickness is decreasing as the heat treatment temperature is increased, and is expected due

to grain growth when the heat treatment temperature is increased. The reason for why the sample heat treated at 850 °C has such a thin layer is because only 5 µg of composite cathode was deposited. For the 950 °C, 1050 °C and 1150 °C samples, the deposited amount of cathode was adjusted to 20 µm to increase the thickness of the layer.

At heat treatment temperature 1050 °C and 1150 °C, the composite cathode has good adhesion to the electrolyte. This is seen by necking between cathode particles and the electrolyte. At 850 °C and 950 °C, adhesion is not easily observed. At 850°C, it is evident from the picture that the particles have fallen of the electrolyte, which also confirms a bad adhesion between the cathode and electrolyte.

Composite B

Fig. 4.5 shows the cross section of the Composite B cathode heat treated at 850°C, 950 °C, 1050 °C and 1150 °C. The thickness and density of the cathode layers are presented in Tab. 4.2. The samples heat treated at 850 °C have a thickness of 2µm, while the samples heat treated at 950 °C, 1050 °C and 1150 °C have a thickness ranging from 6 µm at 950 °C to 3 µm at 1150 °C. The thickness is decreasing with increasing heat treatment temperature due to more grain growth at higher temperatures. Samples heat treated at 1050 °C and 1150 °C show good adhesion to the electrolyte, seen by several neck formations between the cathode particles and electrolyte.

The deposition method resulted in homogeneous and porous cathode layers for all samples. Sufficient SEM-pictures of the samples heat treated at 750 °C was difficult to obtain for both Composite A and Composite B. The cathode material fell of the electrolyte when the samples were handled, confirming that the material did not obtain sufficient adhesion to the electrolyte.

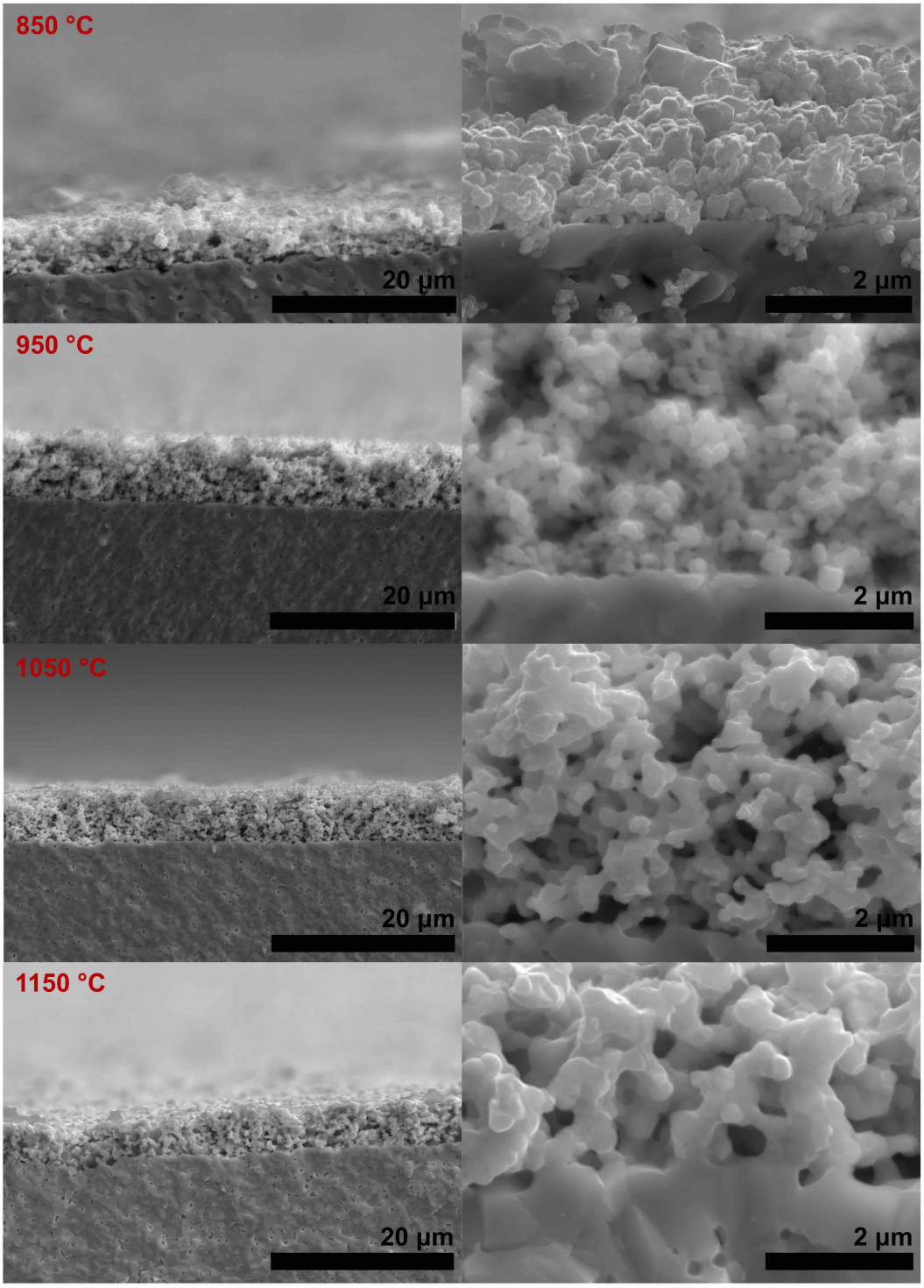

Figure 4.4: SEM images of the cross section of composite A, heat treated at 850 °C, 950 °C, 1050 °C and 1150 °C.

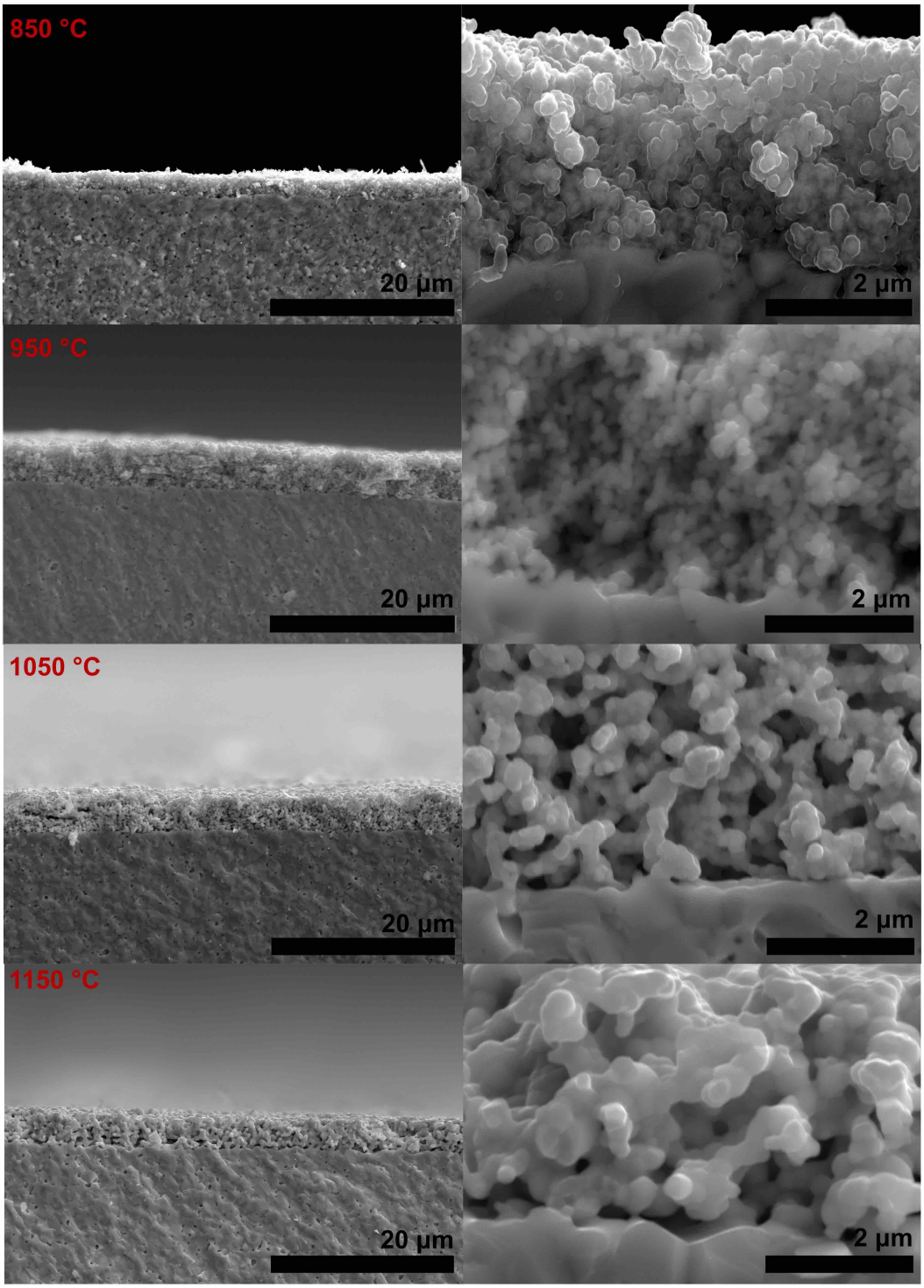

Figure 4.5: SEM images of the cross section of composite B, heat treated at 850 °C, 950 °C, 1050 °C and 1150 °C.

An estimate of the cathode density is calculated, and presented in Tab. 4.2. As the heat treatment temperature is increased, the density of the layers is increasing, which is expected considering that heat is the source for energy that is needed for material transport, inducing grain growth [35].

Table 4.2: Calculated density of composite cathodes, heat treated at 850 °C, 950 °C, 1050 °C and 1150 °C. Calculations can be seen in Appendix in Tab. B.1.

Sample	**Thickness [μm]**	**Density [%]**	**Sample**	**Thickness [μm]**	**Density [%]**
A850	25.3	2.4	**B850**	2.5	28.4
A950	35.4	7.3	**B950**	5.0	51.8
A1050	41.9	6.2	**B1050**	4.3	60.5
A1150	44.8	5.8	**B1150**	3.8	81.6

To get an idea of how well the cathode material was adhering to the electrolyte, a clean, dry Q-tip was wiped across the top surface of cathodes. The results can be seen in Tab. 4.3. Both cathodes show better adhesion with increasing heat treatment temperature, but Composite B start to adhere better at lower temperature compared to Composite A, and achieves better adhesion faster when increasing the heat treatment temperature.

Table 4.3: Test of how well the cathodes adhered to the electrolyte. Each sample was carefully wiped with a clean, dry Q-tip.

Sample	**Adhesion**	**Sample**	**Adhesion**
A650	Easily wiped off	**B650**	Easily wiped off
A750	Easily wiped off	**B750**	Easily wiped off
A850	Better adhesion, but still easily wiped off	**B850**	Better adhesion, but still easily wiped off
A950	Even better, but some comes off	**B950**	No visible cathode on Q-tip
A1050	The Q-tip has **some** trace of cathode	**B1050**	No visible cathode on Q-tip
A1150	No visible cathode on Q-tip	**B1150**	No visible cathode on Q-tip

4.4 Diffusion of cations from cathode to electrolyte

EDS analysis of the cross section of A1050, A1150, B1050 and B1150 was conducted to evaluate the diffusion of cations from the composite cathode into the electrolyte. The element distribution across the cathode-electrolyte interface is presented as line scans in Fig. 4.6.

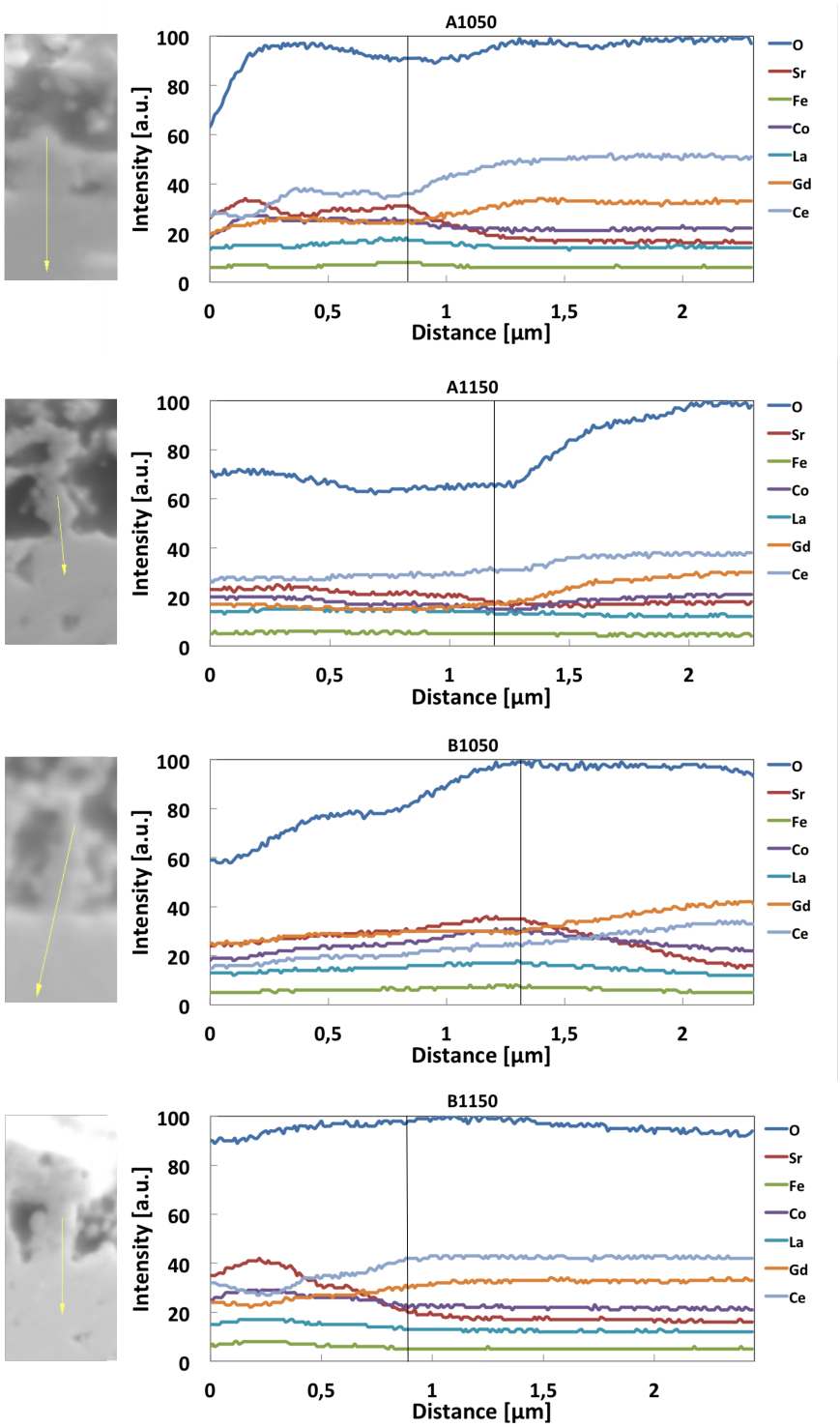

Figure 4.6: Line scan of the interface between composite cathode and electrolyte. The black line in the plots indicates what seems to be the boundary between the two components in the sample. The SEM-recording to the left with the yellow arrow show where in the sample the line scan is conducted.

As seen in Tab. 4.4, all cations diffuse 0.5 to 1 µm into the electrolyte. It seems to be little difference when considering both the temperature and the type of composite, and no significant patterns. The reason for why La, Sr, Co and Fe does not reach zero in the pure CGO electrolyte is because when using EDS scanning. There will always be some background signal, which can be assumed to be noise. The EDS analysis has several restrictions considering the spatial resolution. For elements with a high atomic number, the spatial resolution is 0.2-1 μm^3, which is due to the generation of X-rays occurring very deep in the interaction volume [47]. This means that the measured cation diffusion length can in this case range from 0-2 µm.

Table 4.4: Diffusion length of cations across the interface between composite cathode and electrolyte, calculated from the obtained line scans seen in Fig. 4.6.

Elements	**A1050 [µm]**	**A1150 [µm]**	**B1050 [µm]**	**B1150 [µm]**
Sr	0.7	1	1	1
Fe	0.5	0.5	0.7	0.5
Co	0.5	0.7	1	0.5
La	0.7	0.8	0.8	0.9

4.5 Crystallite size

The top surface of the two samples chosen for impedance spectroscopy was investigated using X-ray diffraction. This was to calculate the crystallite size of LSCF and CGO in the two cathodes. The diffractograms can be seen in Appendix A, Fig. A.1 and Fig. A.2. The crystallite size of the four samples was calculated using Bruker's software Topas [44], and is presented in Tab. 4.5. A plot of the crystallite size as a function of heat treatment temperature can be seen in Appendix A, Fig. A.3.

The crystallites in Composite A grow steadily as the temperature is increased, where CGO obtains larger crystallites compared to LSCF. In Composite B, the difference between the two materials is larger. It seems as if the crystallite growth of LSCF slows down as the temperature is increased above 950 °C. CGO grows significantly more than LSCF. It is difficult to say anything about the grain size of the composites from the crystallite size, due to the fact that a grain might consist of several crystallites.

Table 4.5: Calculated crystallite size of LSCF and CGO in A950, A1050, B950 and B1050. The calculations were conducted in Topas software [44].

Sample	LSCF [nm]	CGO [nm]
A950	29	50
A1050	52	83
B950	50	20
B1050	54	117

4.6 Electrochemical impedance spectroscopy

4.6.1 Oxygen reduction kinetics

Impedance measurements were carried out in dry air atmosphere, following the program presented in Fig. 3.5. The effect of heat treatment temperature was investigated, and Fig. 4.7 and Fig. 4.8 show the data obtained. All data have been normalized to Z_{real}=0 to more easily see the difference in diameter of the semicircles.

The samples heat treated at 950 °C show an evident difference between the two composites, due to the much larger semi-circle diameter for Composite B compared to Composite A. This is the case for all operating temperatures. For the samples heat treated at 1050 °C, the difference in diameter is not as pronounced. The capacitance of the obtained Nyquist-plots are presented in Tab. 4.6, found by using Zview software [46] at the top point of the semi-circles. These values give an indication of what processes are occurring in the symmetric cell [41].

Since the Nyquist-plots show only one pronounced semi-circle, and all capacitance values lie in the range of 10^{-4}-1 F, and values in this range are attributed to the electrochemical reactions occurring in the sample [41].

Table 4.6: The capacitance calculated for each sample at each operating temperature, at the frequency corresponding to the Z(im) top-point [41].

Sample	600 °C	700 °C	800 °C
A950	$1.7 \cdot 10^{-3}$ F	$1.6 \cdot 10^{-2}$ F	1.2 F
B950	$2.2 \cdot 10^{-4}$ F	$5.4 \cdot 10^{-4}$ F	$1.8 \cdot 10^{-3}$ F
A1050	$1.4 \cdot 10^{-2}$ F	$1.8 \cdot 10^{-2}$ F	$3.3 \cdot 10^{-2}$ F
B1050	$2.2 \cdot 10^{-2}$ F	$3.8 \cdot 10^{-2}$ F	$4.5 \cdot 10^{-2}$ F

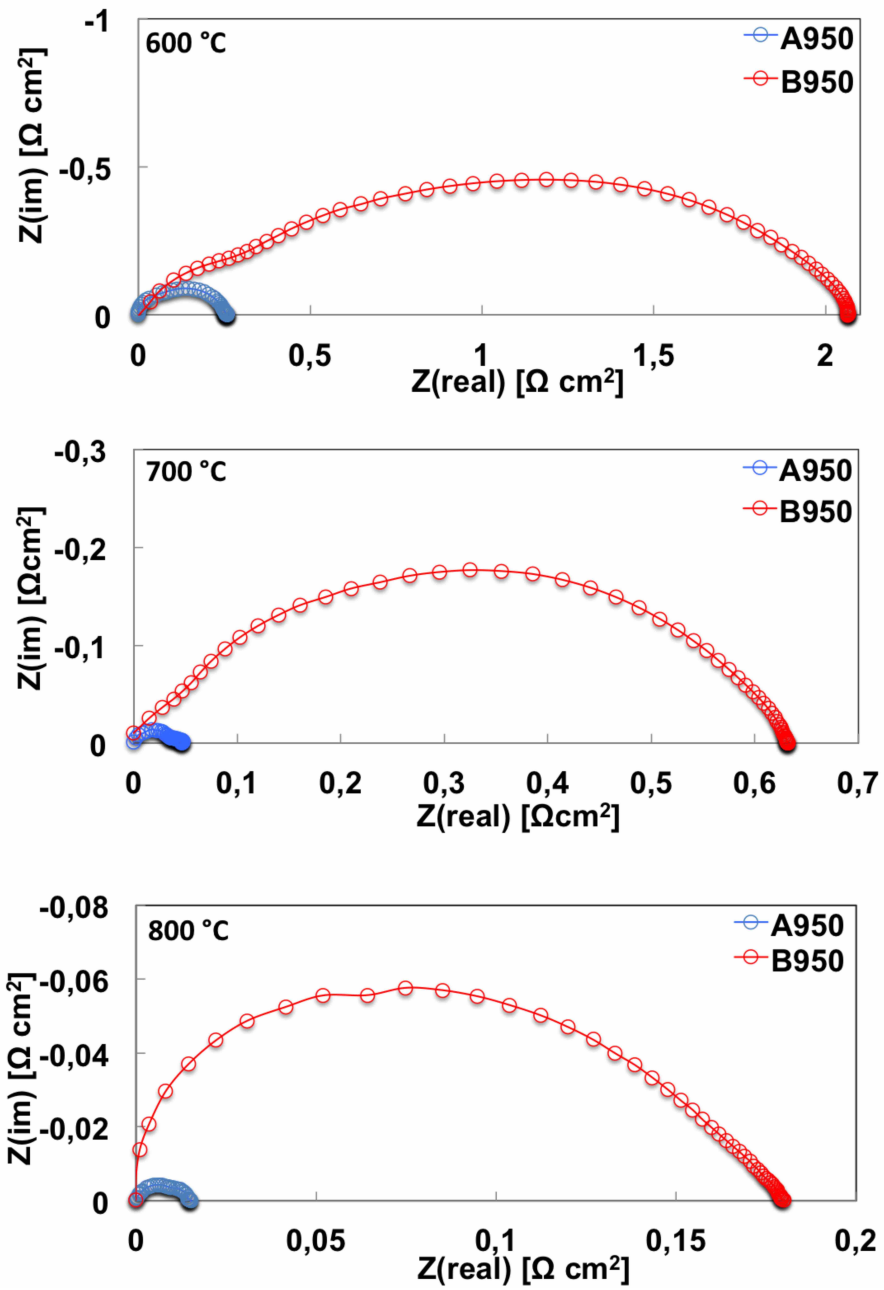

Figure 4.7: Obtained Nyquist-plots of A950 and B950 measured at operating temperature 600 °C, 700 °C and 800 °C. The measurements are conducted in dry air atmosphere.

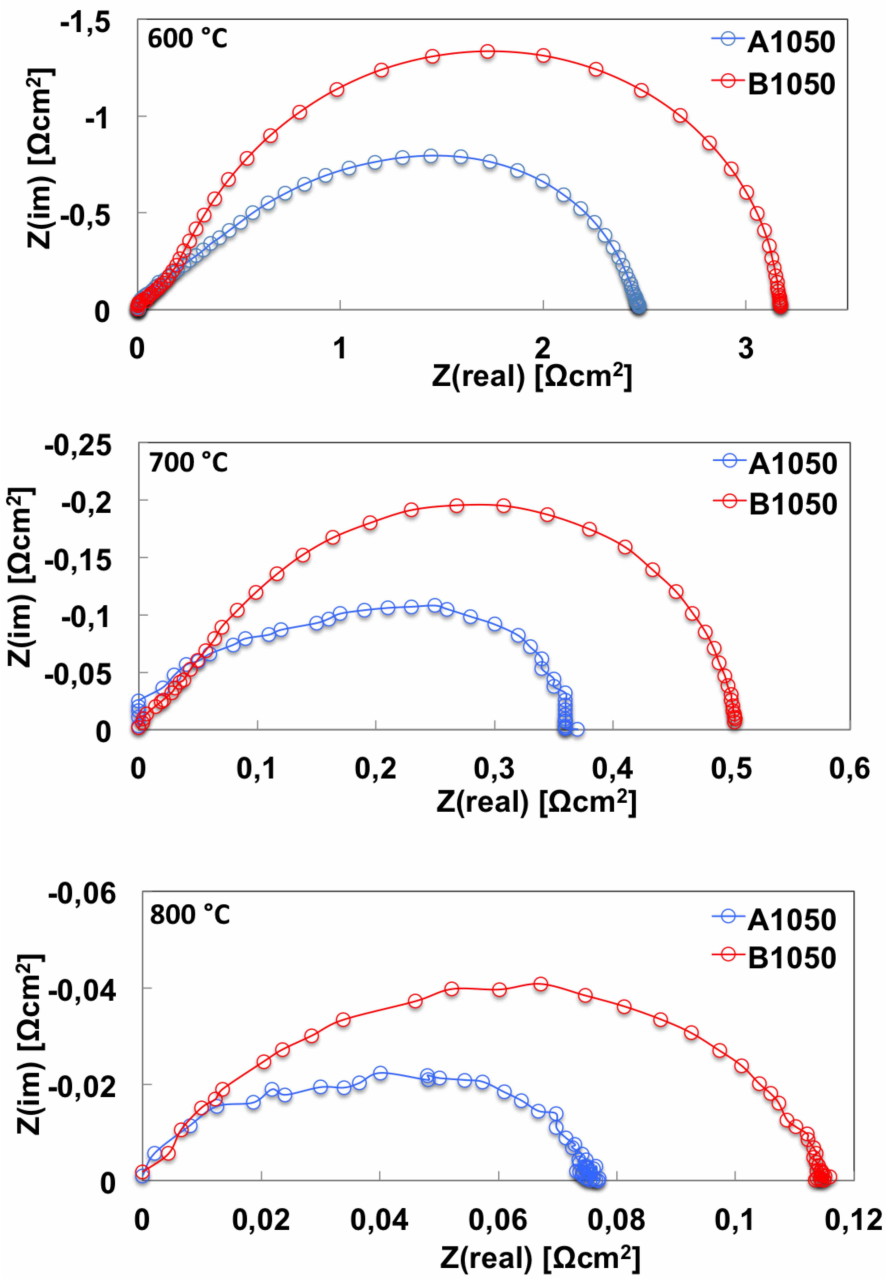

Figure 4.8: Obtained Nyquist-plots of A1050 and B1050 measured at operating temperature 600 °C, 700 °C and 800 °C. The measurements are conducted in dry air atmosphere.

4.6.2 Area specific resistance

The data from the Nyquist-plots have been modeled by the equivalent electrical circuit consisting of a resistor and a constant phase element connected in parallel, representing the kinetics of the electrochemical reaction occurring and the capacitance of the interface, with a resistor in series, representing the ohmic resistance of the electrolyte and wires. From the Nyquist-plots and the use of ZView software [46], the ASR of the two composites heat treated at 950 °C and 1050 °C is obtained. The measurements conducted at 800 °C at the end of the program gave the same values for ASR as the first measurements at 800 °C, indicating that no microstructural changes has occurred in the samples. The curves in the Nyquist-plots are fitted, and the ASR is found as half the diameter of the fitted semi-circles.

Tab. 4.7 presents the obtained values for the ASR, which are plotted in logarithmic scale as a function of operating temperature, seen in Fig. 4.9. The activation energies, also seen in Tab. 4.7, is calculated from the slopes of the plot, using the Arrhenius equation.

As seen from the values in Tab. 4.7 and the graph in Fig. 4.9, the ASR is decreasing as the operating temperature is increased. This is due to the thermally activated oxygen reduction reaction occurring at the surface and movement of oxygen ions through the bulk. The ASR of Composite B, both heat treated at 1050 °C and 950 °C is higher for all running temperatures. Composite A heat treated at 950 °C has a much lower ASR compared to all the other samples.

Table 4.7: The ASR of the two composite cathodes, tested at 600 °C, 700 °C and 800 °C, heat treated at 950 °C and 1050 °C.

ASR [Ωcm^2]	**A1050**	**B1050**	**A950**	**B950**
600 °C	1.39	1.85	0.15	1.18
700 °C	0.22	0.29	0.02	0.36
800 °C	0.05	0.07	0.01	0.1
Activation energy [kJ/mol]	133.4	130.4	105.5	95.5

As seen in Tab. 4.7, the activation energy for both Composite A and Composite B heat treated at 950 °C are close to each other, and the same for both composites heat treated at 1050 °C. It is lower for the samples heat treated at 950 °C, compared to the ones heat treated at 1050 °C.

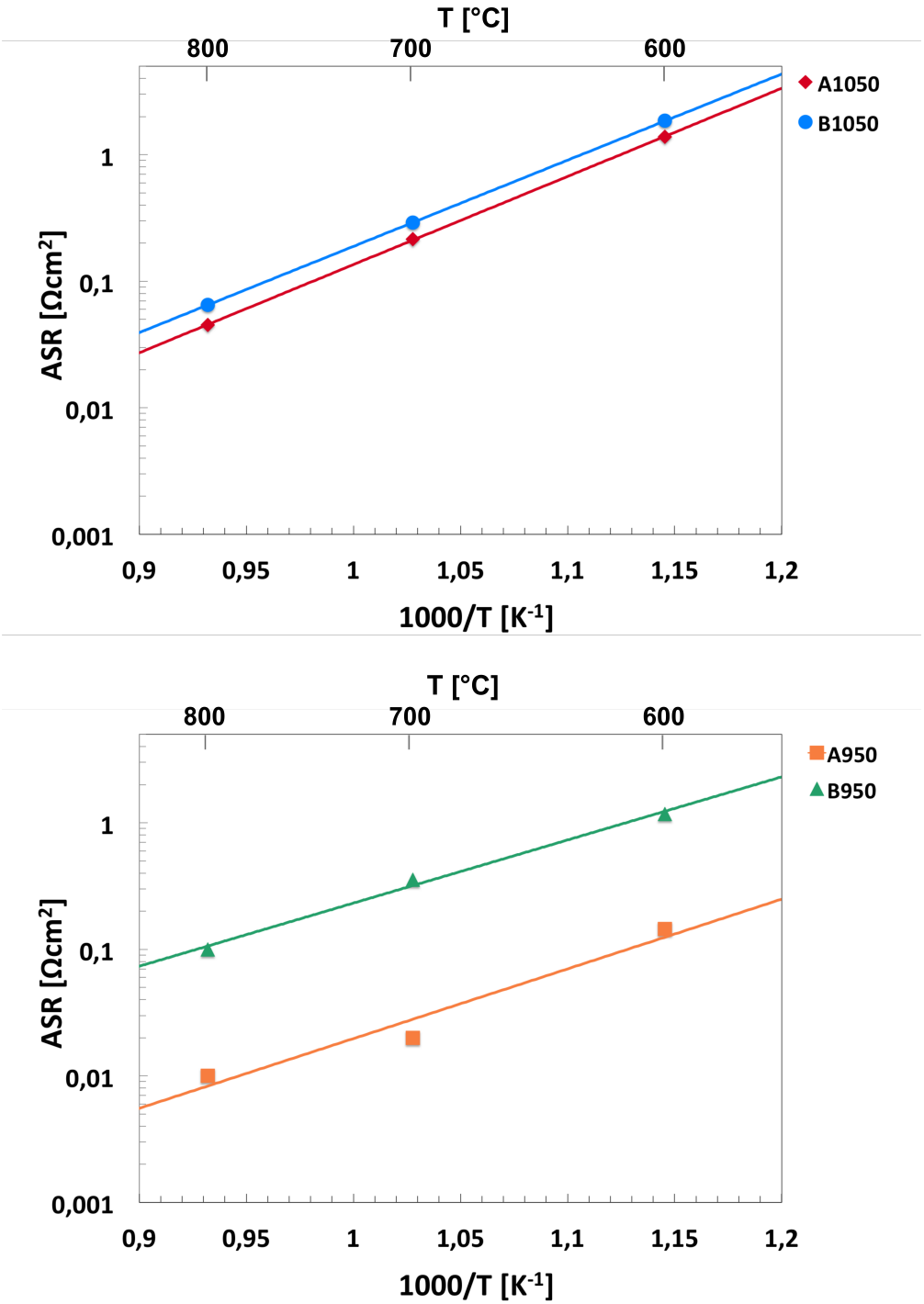

Figure 4.9: The ASR of the four samples, plotted in logarithmic scale as a function of running temperature. The area specific resistance is calculated from the Nyquist-plots. The slope of the curves is the activation energy of the processes occurring in the samples.

4.7 Tested samples

Fig. 4.10 shows SEM images of the four samples after impedance measurements. The thickness of the cathode layers is varying to some extent. A950 has a thickness of around 10 µm, while B950, A1050 and B1050 have a thickness of around 6µm. A950, A1050 and B1050 have an even thickness throughout the cross section of the samples. The thickness of B950 varies across the sample and has a layered structure several places in the cathode. This is probably due to the deposition method.

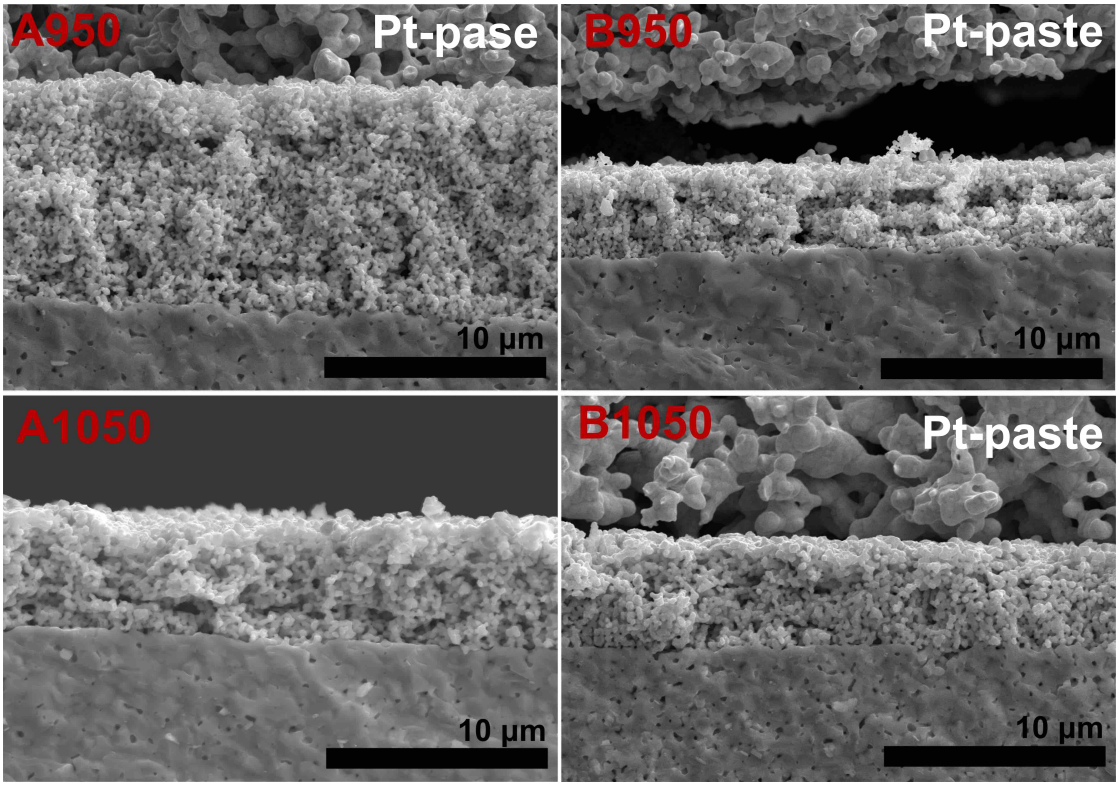

Figure 4.10: SEM recordings of the four tested samples, after impedance measurements.

The density of the tested cathodes is presented in Tab. 4.8. Composite B cathode has a higher density for both heat treatment temperatures.

Table 4.8: Calculated density of tested composite cathodes. Calculations can be found in Appendix in Tab. B.2.

Sample	**Density [%]**	**Sample**	**Density [%]**
A950	28.1	**B950**	46.4
A1050	47.7	**B1050**	63.7

Comparing A950 and B950 after testing in Fig. 4.11, A950 is coarser and contains larger grains. It is evident that the cathode in this sample has sintered to a greater extent compared to B950. By comparing A1050 and B1050, the cathode layers does not look that different from each other in microstructure.

When comparing the microstructure in the samples before and after testing, seen in Fig. 4.11, there is no visible change of microstructure in A1050 and B1050. For A950 and B950, there can seem as if the testes samples have experienced grain growth. The results from the testing at 800 °C at the end of the testing cycle gave the same value for ASR as the first measurements at 800 °C. This indicates that no significant microstructural changes have occurred in the samples during the measurements. The difference seen in the SEM images can be due to bad resolution caused by charging of the samples when conducting SEM-analysis.

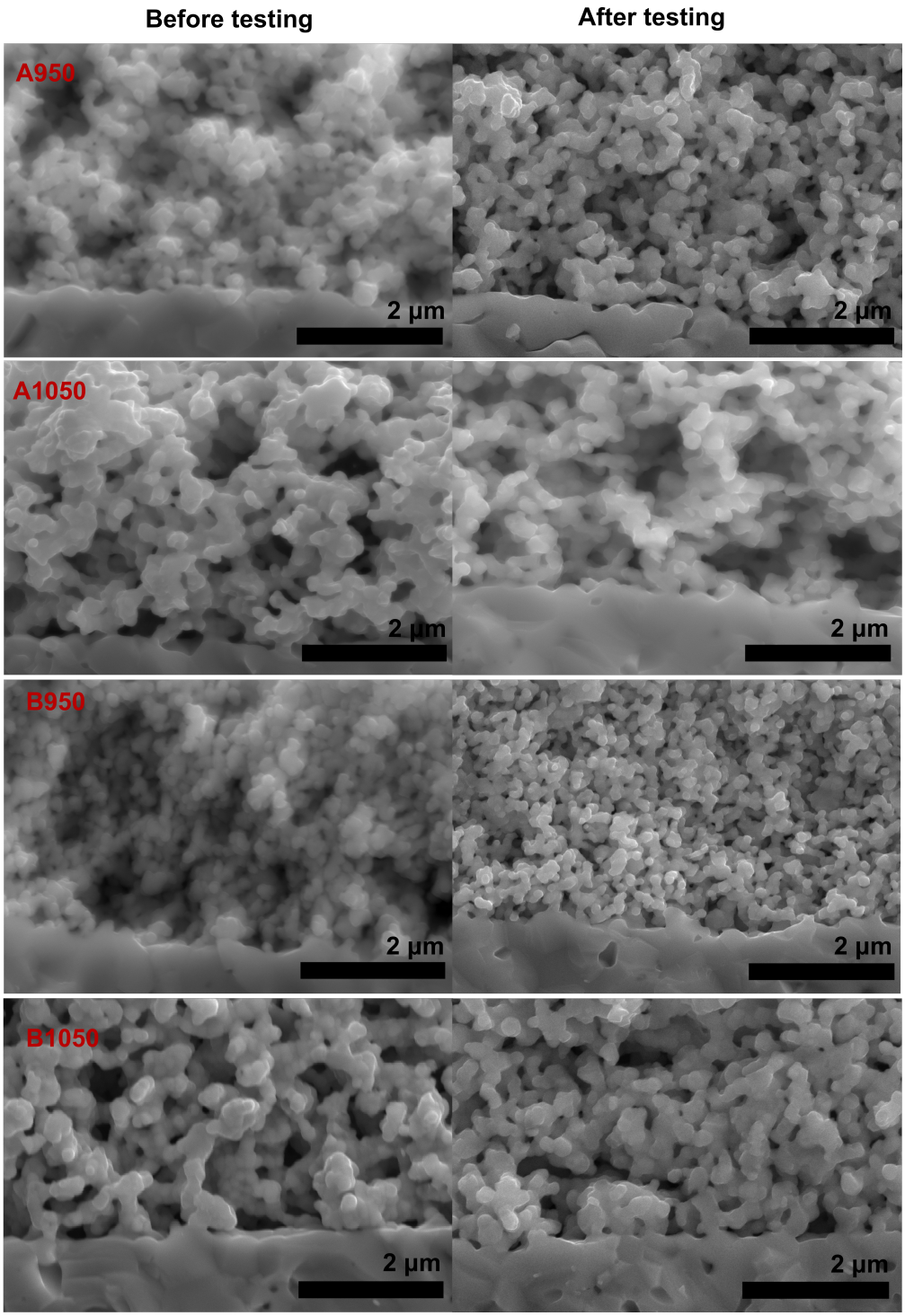

Figure 4.11: SEM images of composite cathodes before and after impedance measurements.

Chapter 5

Discussion

5.1 CGO electrolyte

The CGO pellets were produced using powder produced by spray-pyrolysis, which result nanosized particles. Sintering pellets using such material with a small size-distribution result in high density pellets with small and few pores. This should give an electrolyte that has a high ionic conductivity and perform well as an oxygen ion conductor in a SOFC [8]. The holding time for sintering was 10 hours, producing samples with grain sizes of around 720 nm. By changing holding time and temperature, one could obtain an electrolyte with smaller grains which would give a higher mechanical strength of the component. High mechanical strength is an important factor for a fuel cell in larger scale. At the same time, increasing the number of grain boundaries reduces the ionic conductivity; so larger grains and fewer grain boundaries will enhance the ionic conductivity in the material. Accardo et al. [8] produced CGO pellets with a density of 97 % and grains of 700 nm, with a holding time of 3 hours at 1500 °C. Geisbers [26] found that sintering at higher temperatures and longer holding time will increase the grain size while the density will only slightly increase. To obtain even denser pellets, alternatives could be to increase the sintering temperature from 1300 °C to 1500 °C, and it seems that the holding time could be reduced to 3 hours, to reduce the grain growth.

5.2 Composite cathodes

5.2.1 Sintering properties and thermal expansion

As seen in Fig. 4.3, it is evident that Composite B start to densify at a higher temperature compared to Composite A. Grain growth is seen in Composite B by comparing B750 and B850, and even more comparing these two with B950. By comparing Composite A and Composite B at lower temperatures, Composite A consist of larger particles at both 750 °C and 850 °C, which proposes that Composite A has already experienced coarsening of material prior to production of symmetric cells. This is expected as the dilatometry curve, seen in Fig. 5.1, show that Composite A start to densify at 650 °C, while Composite B start to densify at around 800 °C. This is explained by larger grains in the starting material of Composite B [1], requiring a higher temperature for coarsening and grain growth to initiate. CGO start to densify at 600 °C.

Seen by the slope of the curves in Fig. 5.1, Composite B has a steep slope compared to Composite A, which suggest that Composite B has a more rapid grain growth. These observations support the results observed in the recorded SEM-pictures seen in Fig. 4.3. Composite B goes through a more rapid change in grain size in a smaller temperature range, from B850 to B950, while the particles in Composite A grows slower. Dilatometer curves of Composite A, Composite B and LSCF are obtained during previous work [1].

The TEC was calculated for all four materials from the dilatometry measurements seen in Fig. 5.1, and is presented in Table. 5.1. Composite A has a significantly larger thermal expansion coefficient compared to Composite B, which has a thermal expansion coefficient closer to pure CGO. Giesbers [26] measured thermal expansion coefficients for pure CGO in the range of 13.8-14.8 $\cdot$ 10^{-6}, which are deviating from the results obtained here. Either way, CGO has a TEC matching LSCF better compared to YSZ, which has a TEC around $10 \cdot 10^{-6}$ [11,48]. The obtained results also show that the two composites and CGO have a TEC that does not deviate from each other that much. Karthon et al. [49] report a TEC of 15.4 $\cdot$ 10^{-6} °C^{-1} for LSCF, also different from the results obtained in this research. It is clear that there is a deviation in reported thermal expansion coefficients in literature, which can be due to the temperature range that the TECs are measured

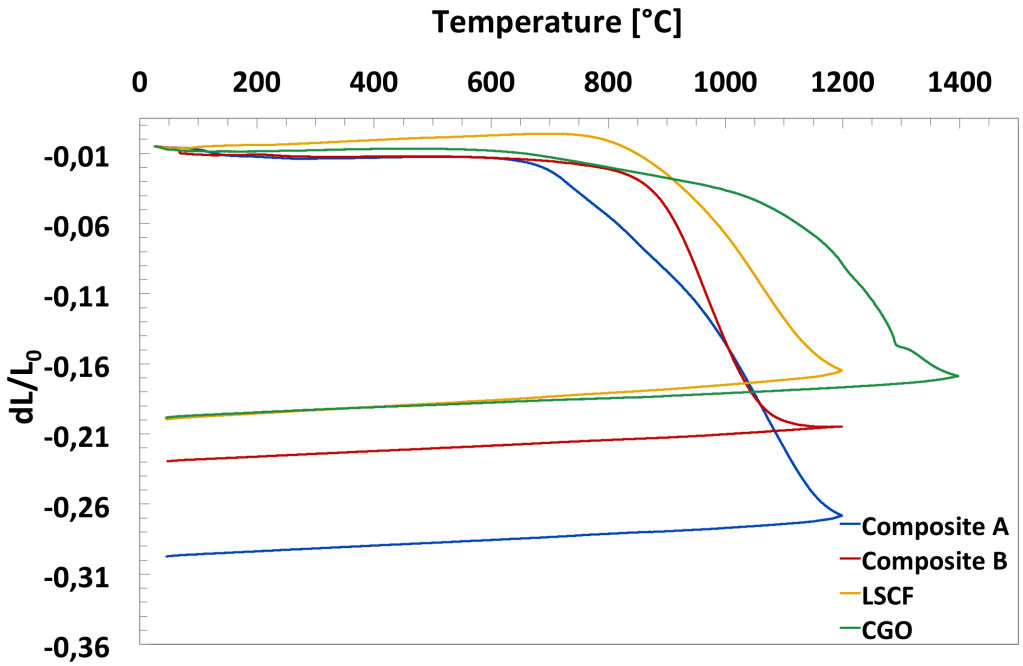

Figure 5.1: Dilatometer curves CGO, LSCF, Composite A and Composite B. Results for Composite A, Composite B and LSCF was obtained in previous work [1]. The program for CGO was set to 1400 °C, for Composite A, Composite B and LSCF it was set to 1200 °C, with a heating and cooling rate of 2 °C/min. The measurements were done in synthetic air atmosphere.

at, differences in the properties of the material, which again can be due to the production route and preparation of the material, and due to uncertainties when measuring the TEC.

Table 5.1: Calculated thermal expansion coefficient (TEC) for Composite A, Composite B, CGO and LSCF.

Material	**TEC [°C^{-1}]**
CGO	$22 \cdot 10^{-6}$
LSCF	$30 \cdot 10^{-6}$
Composite A	$25 \cdot 10^{-6}$
Composite B	$21 \cdot 10^{-6}$

5.2.2 Adhesion of cathode to electrolyte

At temperatures T ≥ 1050 °C, both composite cathodes adhere well to the electrolyte. This is evident in the SEM-pictures recorded of the cross sections of both

Composite A and Composite B, seen in Fig. 4.4 and Fig. 4.5. Neck formation between composite particles and electrolyte is observed several places in the pictures. At 950 °C, it is harder to see clear adhesion between the cathode and the electrolyte, if comparing to the cathodes heat treated at 1050 °C and 1150 °C. High temperature is needed for sintering to occur between particles, and especially between a particle and a dense CGO electrolyte pellet that has been polished. The surface was only polished down to 15 µm, to still have some roughness. At 950 °C, this might not be sufficient for good adhesion. The good adhesion at higher temperature can be due to the high amount of CGO in the cathode, and due to the high heat treatment temperature forcing diffusion of material [35]. What heat treatment temperature to choose for production of symmetric cells will be a compromise between a large surface area with high concentration of triple phase boundaries where the oxygen reduction occurs, and good adhesion to the electrolyte which is important for good ionic conductivity across the interface between cathode and electrolyte. In literature, heat treatment of such systems is usually at temperatures T ≥ 900 °C [50–52], and the purpose of this is not only to obtain a good adhesion to the electrolyte, but also to establish a network structure of the two different materials in the composite cathode to obtain good conductivity [53].

5.2.3 Deposition method

The cathode layers were deposited using an air-brush. This is a non-automatic process, which could give rise to several human errors. The distance from the sample surface to the air-brush, the time between each deposition of cathode material, and the amount of deposited material for each spraying will vary. These factors are hard to avoid, and need to be considered when comparing the four samples tested for electrochemical behavior. Screen-printing is a second method often used for deposition of cathodes [29, 51, 54], but was not considered as the chosen method resulted in homogeneous layers with almost equal thickness across the pellets and few defects.

5.2.4 Cations diffusion from cathode to electrolyte

To evaluate cation diffusion of La, Sr, Co and Fe from cathode into the electrolyte, the cross section of the four samples heat treated at 1050 °C and 1150 °C was in investigated using EDS analysis. When analyzing these results, the value of

the intensity can not be taken into account. Such scans will always give some signals, even though there is no element in the area, and is the reason for why no elements show zero intensity at any point. All elements show diffusion to some extent, varying from 0.5 to 1.2 µm, and is exemplified by the strontium diffusion in Fig. 5.2. The exact value is difficult to find, both since the signal will never go to zero for any element and due to the restriction of spatial resolution of 0.2-1 μm^3 [47]. Considering the size of the CGO-grains, which is found to be around 700 nm, the diffusion of cations into the material is significant for several elements.

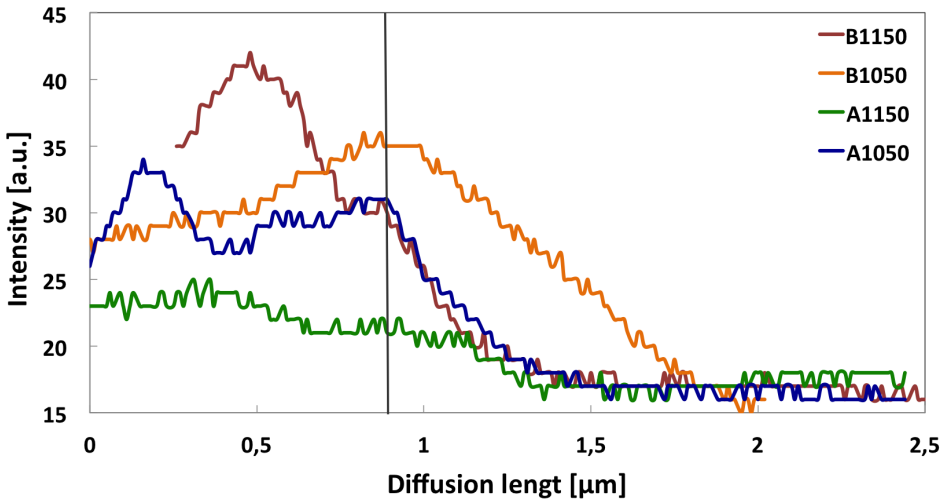

Figure 5.2: The diffusion length of strontium ions from cathode into electrolyte. The black line indicates the start of the diffusion.

Li et al. [39] investigated the interfacial region between LSCF and CGO, heat treated for 2 hours at 1100 °C, and found a mutual diffusion of cations with an average length of 200 nm. The size of the CGO-grains is not reported, neither how the powder or the pellets are produced. Both mutual diffusion between the cathode and electrolyte, and diffusion along grain boundaries was reported, and seems to be of significance as it suggests that the chemical stability between the two materials is not as good as previously reported [39]. Considering that these SOFCs should run for several hours, this is important results to take into consideration.

5.3 Cathode performance

Composite cathodes heat treated at 950 °C and 1050 °C were tested using impedance spectroscopy. This was to investigate the effect of heat treatment temperature on

cathode performance, and also compare the two different composites. The two temperatures were chosen based on the investigation of the cross sections of the samples in SEM. At temperatures T ≥ 1050 °C, good adhesion to the electrolyte was established, seen by necking several places between cathode particles and electrolyte, which is important for oxygen ion transport from the cathode to the electrolyte and for practical purposes. Heat treatment at 950 °C did not show sufficient adhesion in the SEM-pictures, but would have a higher surface area compared to 1050 °C due to less grain growth. The chosen heat treatment temperatures for producing symmetric cells is a compromise between these two parameters, and is why 950 °C and 1050 °C were chosen for impedance spectroscopy.

5.3.1 Oxygen reduction kinetics

All measurements, except for B950 at operating temperature 600 °C, resulted in only one semi-circle for each impedance measurement. This is because the measurements are conducted at higher temperatures, so the semi-circle corresponding to the bulk impedance is not visible at the chosen frequencies and temperatures [41], hence will not show a rate limiting process at these conditions. The capacitance at the frequencies corresponding to the top-points of the semi-circles was calculated to be in the range of 10^{-4} to 1 F for all samples at all operating temperatures, and can be attributed to electrochemical reactions occurring in the sample [41].

For B950, a small bump at higher frequencies can be observed for operating temperature 600 °C, seen in Fig. 4.7. The origin of this is attributed to the sample-electrode interface [41], and was found by calculating the capacitance at this frequency and the corresponding polarization resistance. This limiting process can be due to poor contact between the cathode and platinum electrode for this sample at the current temperature.

Modeling experimental data

The model used to fit the Nyquist-data consisted of one resistor in series with a resistor and a constant phase element in parallel, sketched in Fig. 5.3. This has shown to work well for impedance measured conducted at symmetric cells with MIEC cathodes [43, 50, 55]. All experimental data obtained was fitted using this model. For some of the data recorded at 800 °C and 700 °C, there was noise in the

measurements. An example can be seen in Appendix Fig. C.1. The data-points that was out of place were removed prior to fitting, and gave a good representation of what the curves would look like without the noise. The ASR calculated was still representative for the sample. For further measurements, the voltage was adjusted to remove some of the noise.

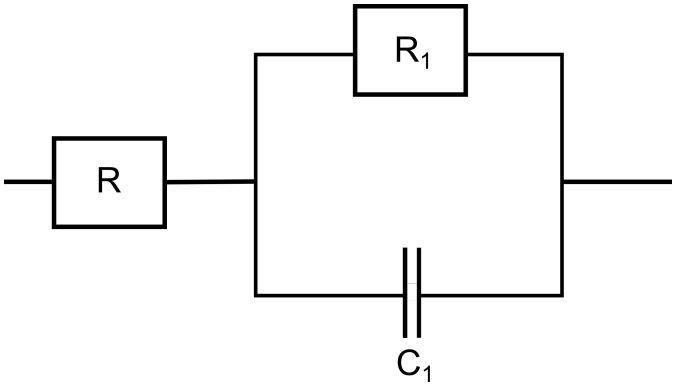

Figure 5.3: Model used to fit the experimental data obtained when conducting impedance spectroscopy.

All curves where fitted using the model described, and an example of a fitted curve is seen in Appendix, Fig. C.2. For all raw data, the model was evaluated by comparing the curve with the experimental data and seemed to fit for all samples, especially at the operating temperature of 600 °C. At higher temperatures, the noise made it hard to obtain a smooth curve, but was evaluated to fit these sufficiently.

For B950 at operating temperature 600 °C, there could have been added a second RC-element when modeling the results from the impedance measurements. A sketch can be seen in Fig. 5.4. The Nyquist-plots seemed to have a second semi-circle at high frequencies implying that a second process was occurring during measurements. The capacitance of this second semi-circle was acquired to the sample-electrode interface. Since this was due to bad contact between the Pt-paste and the process of the electrochemical reactions were still well represented by the fitting, the modeling without a second RC-element was found satisfactory. But, as seen in Fig. 5.4, if two RC-elements are used, the ASR of the large semi-circle is reduced. This is important to take into account when evaluating the ASR results. Adding a second RC element was not conducted for all measurements due to time limitation.

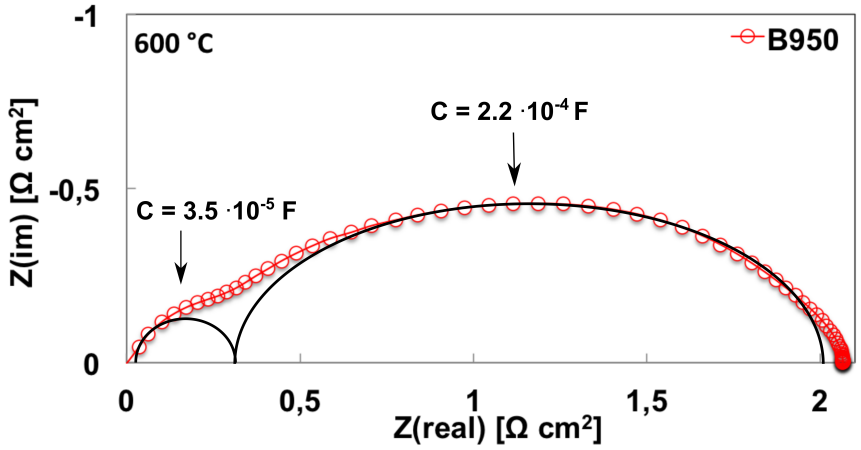

Figure 5.4: Sample B950 modeled with two RC-elements, with the associated capacitance.

5.3.2 Area specific resistance

The area specific resistance was calculated as half the diameter of the semi-circles, and plotted as a function of operating temperature.

Synthesis method

As seen by the plot in Fig. 5.5, composite A had a smaller ASR for both heat treatment temperatures compared to Composite B. Composite A is directly spray-pyrolysed, consisting of an intimate mixture of CGO and LSCF particles, which gives rise to a higher concentration of active sites where the oxygen reduction reaction can occur. Even though the grains in Composite A look larger compared to Composite B, seen in Fig. 4.10, the crystallites in Composite A plays an important role. Each grain in Composite A consist of both LSCF and CGO crystallites [33, 34], hence across the surface area of one grain in Composite A, crystallites of LSCF and CGO meet, giving TPBs. This will give rise to a larger concentration of reaction cites in Composite A compared to Composite B. Also, the porosity of the Composite A cathodes might be closer to ideal porosity, giving a better oxygen gas flux. The calculated density of the tested samples show that Composite A has a lower density for both temperatures, 28.1 % and 47.7 % for 950 °C and 1050 °C, respectively. Composite B has higher density for each heat treatment temperature, 46.4 % and 63.7 % for 950 °C and 1050 °C, respectively, which might impact the oxygen flux in the cathode, contributing to the large ASR

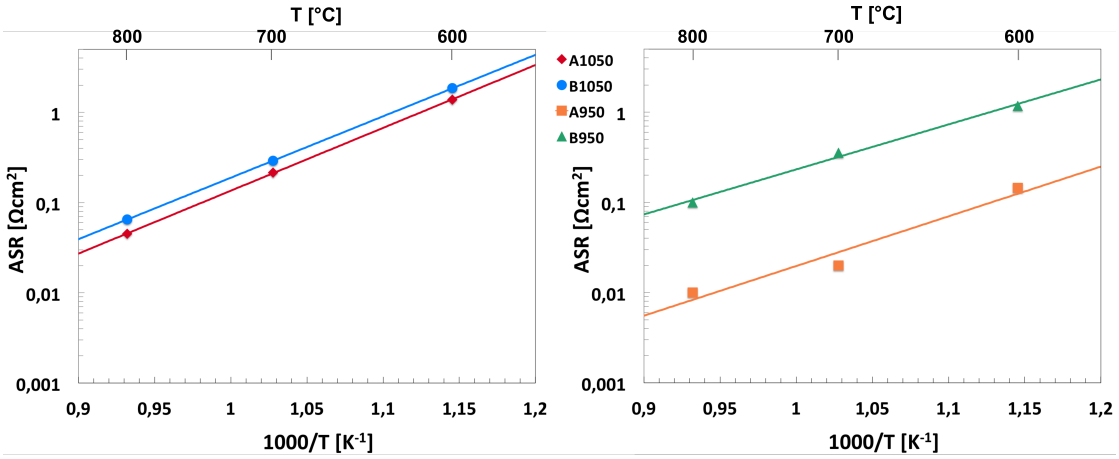

Figure 5.5: Area specific resistance for composite cathodes heat treated at 950 °C and 1050 °C.

compared to Composite A.

At heat treatment of 950 °C, the difference in ASR between the two composites is significant for all operating temperatures, seen in Fig. 5.5. Considering the sintering kinetics of the two composites seen in Fig. 2.15, Composite A has sintered slightly more at 950 °C than Composite B, suggesting that Composite A might have obtained better contact between the particles in the cathode at this temperature, leading to better paths for oxygen ions to travel through the cathode to the electrolyte. At the same time, the low temperature has limited the grain growth and the composite still contains a high number of TPB.

The difference between A950 and B950 can also be due to the cathode thickness. As seen in Fig. 4.10, B950 consist of a thinner cathode compared to A950. A thin cathode gives a smaller number of TPB, which will increase the overall resistance. On the other hand, a cathode that is too thick will have a high concentration of TPB, but the distance from the reaction point to the electrolyte for the oxygen ions to travel will be large. A compromise between a large number of TPB and cathode thickness is necessary, finding the ideal thickness that will give the lowest ASR. A threshold thickness is found as 10-15 times the particle size in the material [34]. For A950, this is calculated to be 3.7-5.6 µm, while for B950 this is 2.9-4.4 µm, based on the grain size of the composite cathodes in Fig. 4.3. The thickness of the tested sample of A950 was 10.9 µm, and for B950 it was 5.6 µm. For A950, this is far from ideal, while for B950, the thickness is close to ideal. B950 varied a lot in thickness across the sample and consisted of a layered structure several places, seen in Fig. 5.6. Such defects were not seen in either of the three other samples, and might have reduced the concentration of TPB. One should also consider the density of the cathodes, discussed earlier.

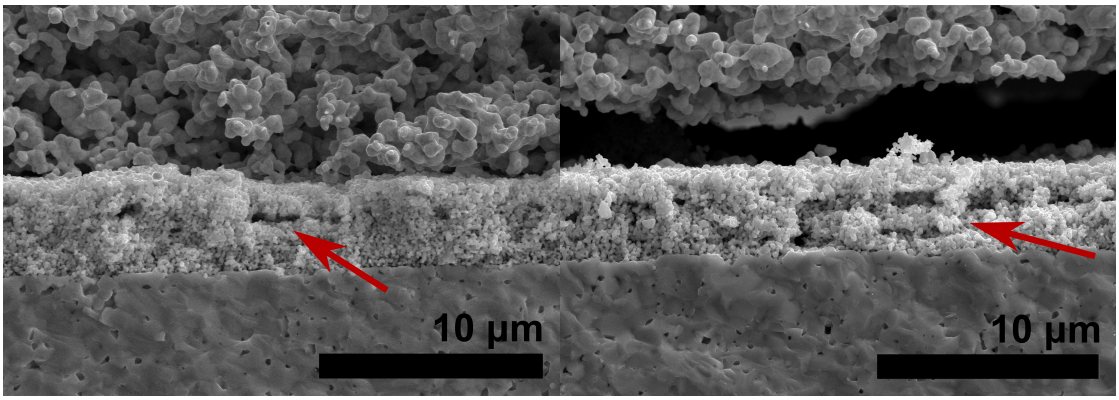

Figure 5.6: SEM recordings of B950, tested cathode, with visible layered microstructure.

At 1050 °C, both composites have sintered well and experienced grain growth. They seem to have roughly the same grain size when investigating the SEM-recordings in Fig. 4.10. The difference in microstructure between Composite A and Composite B at this temperature is not significant; hence the difference in ASR may not be due to a large difference in surface area. The small difference in ASR can be due that one grain in Composite A consist of an intimate mixture of both CGO and LSCF, while one grain in Composite B consist of either CGO or LSCF, giving a lower concentration of TPB. Composite B at 950 °C is comparable to A1050 and B1050, suggesting that the mechanically mixed material has a low

density of TPB even at lower heat treatment temperatures. A950 is the sample standing out, and since Composite B heat treated at 950 °C has a much higher ASR, the low ASR for A950 is probably due to synthesis method.

Shimada et al. [53] produced composite cathodes consisting of 70 % Sm-doped CeO_2 (SDC) and 30 % Sr-doped $SmCoO_3$ (SSC) sintered at 950 °C, which had an ASR of 0.23 Ωcm^2 at 600 °C operating temperature. This included the anode polarization resistance, hence the ASR for the cathode would be even smaller. The cathode that was sintered at 950 °C showed the highest power density output, so this was decided to be the optimal sintering temperature for these cathodes. This was attributed to the high ionic and electronic conductivity in the cathode, because of the obtained network structure between the two composite materials, but still contained a large surface area and a high concentration of TPBs. Comparing with this study, the low ASR obtained for A950 can be attributed to this.

An ASR value of 10.1 Ωcm^2 at operating temperature 600 °C was reported in Zhang et al.'s work [34] for CGO-LSM cathodes sintered at 900 °C. This was a remarkably larger resistance compared to the results obtained in this work. The CGO-LSM composite had a one to one molar ratio, which suggests that the amount of ionically conducting phase in the cathode is not sufficient. Also, the network structure discussed earlier might not have developed at this heat treatment temperature. At operating temperature 700 °C, the ASR was reduced to 2.6 Ωcm^2 [34], which is still large when comparing to the results obtained here.

Heat treatment temperature

As seen in Fig. 5.5, higher heat treatment temperature of the cathodes gives rise to a larger ASR for both composites. This is due to grain growth and crystallite growth in the material during heat treatment at higher temperatures, giving a reduction in surface area. The heat treatment temperature is a compromise between good adhesion to the electrolyte and a large surface area which will give rise to a greater number of reaction cites for the oxygen reduction. In this case, heat treatment at 950 °C seems to give sufficient adhesion to the electrolyte at the same time as a good network structure is developed, seeing that at this heat treatment temperature the ASR is significantly lower comparing to heat treatment at 1050 °C.

Zhang et al. [34] found that for symmetric cells heat treated at lower temperatures, the ASR was reduced. Cathodes heat treated at 700 °C obtained an ASR of 1.22 Ωcm^2 at operating temperature 600 °C, compared to higher ASR values for cathodes heat treated at higher temperatures. This emphasizes the importance of a large surface area, and how much this affects the resistance in the cell. In this research, testing cells heat treated at lower temperatures could give even lower ASR values, seeing the trend in Zhang et al.'s work [34].

Operating temperature

The ASR is plotted as a function of operating temperature to easily see the change in resistance with temperature. For all samples, the ASR is reduced when the temperature is increased, which is expected due to the thermal dependency of the oxygen reduction reaction [26].

The results obtained for the composite cathodes are plotted and compared to the results obtained for pure LSCF cathode in [28], presented in Fig. 5.7. The interesting part here is the large difference at 600 °C between the pure LSCF cathodes and the composite cathodes. Composite A heat treated at 950 °C has a significantly lower ASR compared to all other cathodes.The ASR at 600 ° for A950 is 0.15 Ωcm^2, while for pure LSCF heat treated at 950 °C, the ASR is 2.52 Ωcm^2.

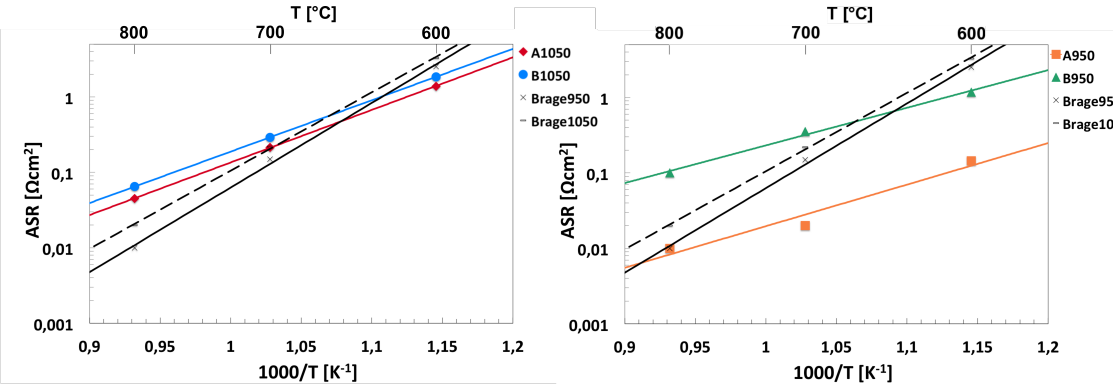

Figure 5.7: Obtained results for Composite A and Composite B, compared with results from Brage Kjeldby's master thesis for pure LSCF cathodes [28]

At 800 °C, the interesting part is comparing B950, B1050 and A1050 with pure LSCF cathode. At this operating temperature, pure LSCF has a lower ASR compared to these three composite cathodes. At operating temperature 800 °C, LSCF

has a higher ionic conductivity compared to CGO. Since the composite cathodes contain only 30 % LSCF, this might not be sufficient for good overall ionic conduction in the composite cathode at higher temperature and the ASR is significantly reduced compared to pure LSCF. This suggests that the effect of composite cathodes will only take effect at lower operating temperatures.

5.3.3 Activation energy

As presented in Tab. 4.7, the activation energies for the different composites at each heat treatment temperature are comparable, and at each heat treatment temperature, Composite B has a lower activation energy compared to Composite A. It is clear that the main influencing factor of activation energy is the heat treatment temperatures of the cathodes, due to the large difference in activation energy between the two heat treatment temperatures. The synthesis route is also influencing the activation energy to some extent.

The activation energy gives important information about the processes occurring in the cathodes. Through impedance spectroscopy, the technique is able to separate between the different reaction steps taking place in the sample. By measuring the impedance as a function of temperature, the ASR can be plotted in an Arrhenius-plot and the slope of the plots represent the activation energy, originating from all the cathode processes occurring in the sample [56]. Seeing that all measured ASR values lie in a straight line, suggests that the same process is the limiting one at all temperatures.

To evaluate the calculated activation energies for the composite cathodes, the activation energies reported for oxygen surface exchange and for oxygen self-diffusion in both CGO and LSCF should be taken into account. The activation energy for the oxygen surface exchange is reported to be 113 $\pm$ 11 kJ/mol [57] and 175 kJ/mol [58] for LSCF and CGO, respectively. The activation energy for oxygen self-diffusion is reported to be 200 kJ/mol for LSCF [59] and 128 kJ/mol for CGO [58]. The reason for the difference in diffusion coefficients of the two materials is because the diffusion of oxygen in the bulk of a fluorite phase occurs much easier than in the perovskite structure [60]

The calculated activation energies for the composite cathodes are in good accordance with the activation energies for the oxygen surface exchange process of LSCF [57]. A950 and B950 has an even lower activation energy than this, which can be due to the addition of CGO. The well-dispersed, intimate mixture of the two materials increases the concentration of TPBs and enhances the ionic conductivity of the cathodes, which leads to a decrease in activation energy. As found in Zhou et al.'s work [56], LSCO/CGO composite cathodes had lower activation energies, compared to pure LSCO. The addition of CGO extended the chemically active sites, expanding the number of TPBs, giving an enhanced oxygen reduction reaction in the composite cathodes [56]. Darbandi et al. [50] also reported a reduction in activation energy when comparing pure LSCF cathodes with LSCF/CGO composite cathodes. An activation energy of 141.7 kJ/mol for LSCF cathodes, and a value of 109.1 kJ/mol for composite cathodes consisting of 10 % CGO was reported [50]. These results emphasize the importance of the bulk process of oxygen conduction. The activation energy is strongly reduced in composite cathodes consisting CGO, having a high ionic conductivity at lower temperatures. The contribution of bulk diffusion to the value of activation energy is strongly reduced by the enlarged surface area of TPB and shorter diffusion paths from the cathode surface to the electrolyte.

The activation energy is higher for both samples heat treated at 1050 °C, getting closer to the value of oxygen self-diffusion of 200 kJ/mol for LSCF [59], but still lower. Higher heat treatment temperatures reduce the surface area and concentration of TPB in the surface. It is reasonable to believe that the increase in activation energy is due to a smaller available area for the oxygen reduction to occur. Benel et al. [61] found for pure LSM cathodes that the activation energy decreased with increasing heat treatment temperature, and was attributed to the improved oxygen ion conductivity for cathodes heat treated at higher temperatures that had obtained a better particle connectivity. This was also reported in Brage Kjeldby's master's thesis [28], and is the opposite of what is occurring in the composite cathodes. For composite cathodes, the activation energy seems to reach a minimum with decreasing temperature, at a certain temperature, and increasing again when further decreasing the temperature [62]. This can be due to a trade off when it comes to a large surface area with a high density of TPBs where the oxygen reduction reaction can occur, and a good connectivity between the two

materials in the composite cathode. In this research, the activation energy might have increased for heat treatment temperatures T ≤ 950 °C.

Bulk processes is dominating for thick cathodes, while surface exchange processes dominate in thinner cathodes. When considering the thickness of the tested cathodes, compared to the calculated ideal thickness, it is reasonable to believe that the thickness of the cathodes contributes to an increase in activation energy, since both had a larger thickness than the calculated ideal thickness. When comparing Composite A and Composite B, Composite B is thinner for both 950 °C and 1050 °C, which might also explain the lower activation energy value for Composite B, suggesting that at thinner cathode is more ideal in this case.

It is difficult to draw any conclusions for what process is rate-limiting in the samples tested in this thesis. Several processes is occurring in the symmetric cell, but by measuring impedance response as a function of oxygen partial pressure, more information about the rate-limiting steps can be found. The ASR is proportional to $pO_2{}^{-n}$, and by plotting natural logarithm of the ASR values, as a function of the natural logarithm of the oxygen partial pressure, n can be found which is associated with different rate-limiting steps occurring. n=0 if the rate-limiting step is the oxygen ion bulk diffusion or transport of oxygen ions from cathode to electrolyte, n=0.5 for dissociative adsorption or diffusion and n=1 when the rate-limiting step is the oxygen gas diffusion or non-dissociative adsorption [63, 64].

5.4 Further work

For further work, several samples at each heat treatment temperature should be tested, to correct for errors and improve the credibility of the research. Several sources of error could have affected the obtained results, and these should be reduced by obtaining more statistics.

Spray-pyrolysed composite cathodes heat treated at even lower temperatures should be further investigated. This is based on literature data, where several researchers

have conducted impedance measurements on cathodes heat treated at low temperatures and have obtained good values for ASR. The effect of holding time when heat treating the composite cathodes could also be optimized. To investigate the different rate-limiting processes occurring in the samples further, the effect of oxygen partial pressure could be tested.

Chapter 6

Conclusion

Two synthesis methods and sintering temperatures for producing composite based cathodes were successfully investigated using impedance spectroscopy. The measurements were conducted in dry air atmosphere at 600 °C, 700 °C and 800 °C. Both consisted of 70 % $Ce_{0.9}Gd_{0.1}O_{2-\delta}$ and 30 % $La_{0.6}Sr_{0.4}Co_{0.2}Fe_{0.8}O_{3-\delta}$. Composite A, which was spray-pyrolysed, had a lower ASR for all operating temperatures compared to Composite B, the mechanically mixed composite. This was ascribed to the synthesis method giving a higher density of triple phase boundaries in Composite A. The ASR was increased when increasing the heat treatment temperature from 950 °C to 1050 °C, and was due to the reduction of surface area giving a lower concentration of triple phase boundaries. The heat treatment temperature should be kept low to obtain a large surface area, as long as this not impacts the adhesion of cathode to the electrolyte. The activation energy was calculated for all samples, and was low compared to literature values. Heat treatment at 950 °C gave a lower activation energy compared to heat treatment at 1050 °C. The limiting process seemed to be more controlled by the oxygen exchange reduction reaction at the surface. The obtained results are promising for the use of composite based cathodes, produced by spray-pyrolysis, in SOFCs running at lower operating temperatures.

Bibliography

[1] Maria Angeltveit. *Development of next generation cathodes for solid oxide fuel cells*. PhD thesis, 2016.

[2] O. Edenhofer, R. Pichs-Madruga, Y. Sokona, J. C. Minx, E. Farahani, K. Susanne, K. Seyboth, A. Adler, I. Baum, S. Brunner, P. Eickemeier, B. Kriemann, J. Savolainen, S. Schlomer, C. von Stechow, and T. Zwickel. Climate Change 2014: Mitigation of Climate Change. Technical report, 2014.

[3] M. Denchak. Are the Effects of Global Warming Really that Bad?. https://www.nrdc.org/stories/are-effects-global-warming-really-bad. Accessed: 18.09.2016.

[4] UNFCC. The Paris Agreement . http://unfccc.int/paris_agreement/items/9485.php. Accessed: 13.12.2016.

[5] E. D. Wachsman and K. T. Lee. Lowering the Temperature for Solid Oxide Fuel Cells. *Science*, 334(6058):935–939, 2011.

[6] S. J. McPhail, V. Cigolotti, and A. Moreno. Fuel cells in the waste-to-energy Chain. In *Green Energy and Technology*, volume 45, pages 109–122. 2012.

[7] Theo Elmer, Mark Worall, Shenyi Wu, and Saffa B. Riffat. Fuel cell technology for domestic built environment applications: State of-the-art review. *Renewable and Sustainable Energy Reviews*, 42(1):913–931, 2015.

[8] Grazia Accardo, Claudio Ferone, Raffaele Cioffi, Domenico Frattini, Luca Spiridigliozzi, and Gianfranco Dell'Agli. Electrical and microstructural characterization of ceramic gadolinium-doped ceria electrolytes for ITSOFCs by sol-gel route. *Journal of applied biomaterials & functional materials*, 14(1):35–41, 2016.

[9] R. P. Reolon, C. M. Halmenschlager, R. Neagu, C. De Fraga Malfatti, and C. P. Bergmann. Electrochemical performance of gadolinia-doped ceria (CGO) electrolyte thin films for ITSOFC deposited by spray pyrolysis. *Journal of Power Sources*, 261(1):348–355, 2014.

[10] Wang Hay Kan and Venkataraman Thangadurai. Challenges and prospects of anodes for solid oxide fuel cells (SOFCs). *Ionics*, 21(2):301–318, 2014.

[11] S. C. Singhal. Advances in solid oxide fuel cell technology. *Solid State Ionics*, 135(1-4):305–313, 2000.

[12] N. Preux, A. Rolle, and R. N. Vannier. *Electrolytes and ion conductors for solid oxide fuel cells (SOFCs)*. Woodhead Publishing, 1st edition, 2012.

[13] A.R. West. *Basic Solid State Chemistry*. John Wiley & Sons, 2nd edition, 2012.

[14] A. J. Jacobson. Materials for solid oxide fuel cells. *Chemistry of Materials*, 22(3):660–674, 2010.

[15] Cahit Benel. *Nanotructured Electrodes for Low Temperature Solid Oxide Fuel Cells*. PhD thesis, Technische Universitat Darmstadt, 2016.

[16] K. Momma and F. Izumi. VESTA 3 for three-dimensional visualization of crystal, volumentric and morphology data, 2011.

[17] H. J. M. Bouwmeester. Dense ceramic membranes for methane conversion. *Catalysis Today*, 82(1-4):141–150, 2003.

[18] S. P. Jiang. A comparison of O2 reduction reactions on porous (La,Sr)MnO3 and (La,Sr)(Co,Fe)O3 electrodes. *Solid State Ionics*, 146(1-2):1–22, 2002.

[19] V. Dusastre and J. A. Kilner. Optimisation of composite cathodes for intermediate temperature SOFC applications. *Solid State Ionics*, 126(1):163–174, 1999.

[20] Ji. Zhang and H. Li. Perovskite: Crystallography, Chemistry and Catalytic Performance. chapter 3, pages 98–118. Nova Science Publishers, New York, 2013.

[21] Ø. F. Lohne. Stability and oxygen transport properties of B-site substituted Lanthanum strontium ferrite. (September), 2013.

[22] L. W. Tai, M. M. Nasrallah, H. U. Anderson, D. M. Sparlin, and S. R. Sehlin. Structure and electrical properties of La(1-x)SrxCo(1-y)FeyO3. Part 2. The system La(1-x)SrxCo0.2Fe0.8O3. *Solid State Ionics*, 76(3-4):273–283, 1995.

[23] L. W. Tai, M. M. Nasrallah, H. U. Anderson, D. M. Sparlin, and S. R. Sehlin. Structure and electrical properties of La(1-x)SrxCo(1-y)FeyO3. Part 1. The system La0.8Sr0.2Co(1-y)FeyO3. *Solid State Ionics*, 76(3-4):259–271, 1995.

[24] V. Øygarden. *4d/5d Transition Metals in Perovskite Cathode Materials*. Phd thesis, Norwegian University of Science and Technology, 2013.

[25] S. Sr, Co Cu, O L, Y. Fu, J. Ouyang, C. Li, and S. Hu. Cathodes for Solid Oxide Fuel Cells. volume 7, pages 1–9. 2012.

[26] Arjen Giesbers. *Development of cathodes for low temperature solid oxide fuel cells Oxygen reduction mechanism*. PhD thesis, 2004.

[27] S. Wang, M. Katsuki, M. Dokiya, and T. Hashimoto. High temperature properties of La0.6Sr0.4Co0.8Fe0.2O(3-δ) phase structure and electrical conductivity. *Solid State Ionics*, 159:71–78, 2003.

[28] Brage Braathen Kjeldby. Effect of Firing Temperature on the Kinetics of Oxygen Reduction in LSCF Cathodes for Solid Oxide Fuel Cells. (June), 2015.

[29] S. B. Adler. Factors governing oxygen reduction in solid oxide fuel cell cathodes. *Chemical Reviews*, 104:4791–4843, 2004.

[30] Neil L. Robertson and James N. Michaels. Oxygen Exchange on Platinum Electrodes in Zirconia Cells: Location of Electrochemical Reaction Sites. *Journal of The Electrochemical Society*, 137(1):129, 1990.

[31] O Yamamoto. Perovskite-type oxides as oxygen electrodes for high temperature oxide fuel cells. *Solid State Ionics*, 22(2-3):241–246, 1987.

[32] N. H. Behling. *History of Solid Oxide Fuel Cells*. 2013.

[33] Hiroyuki Shimada, Toshiaki Yamaguchi, Hirofumi Sumi, Katsuhiro Nomura, Yuki Yamaguchi, and Yoshinobu Fujishiro. Extremely fine structured cathode for solid oxide fuel cells using Sr-doped LaMnO3 and Y2O3-stabilized

ZrO2 nano-composite powder synthesized by spray pyrolysis. *Journal of Power Sources*, 341:280–284, 2017.

[34] Lei Zhang, Liangzhu Zhu, and Anil V. Virkar. Nanostructured Cathodes for Solid Oxide Fuel Cells by a Solution Spray-Coating Process. *Journal of The Electrochemical Society*, 163(13):1358–1365, 2016.

[35] D. W. Richerson. *Modern Ceramic Engineering*. 3rd edition, 2006.

[36] T. Mokkelbost, Ø. Andersen, R. A. Strøm, K. Wiik, T. Grande, and M. A. Einarsrud. High-temperature proton-conducting LaNbO4-based materials: Powder synthesis by spray pyrolysis. *Journal of the American Ceramic Society*, 90(11):3395–3400, 2007.

[37] S. Jain, D.J. Skamser, and T. T. Kodas. Morphology of single-component particles produced by spray pyrolysis. *Aerosol Science and Technology*, 27(5):575–590, 1997.

[38] Ye Lin, Shumin Fang, Dong Su, Kyle S Brinkman, and Fanglin Chen. Enhancing grain boundary ionic conductivity in mixed ionic-electronic conductors. *Nature communications*, 6:6824, 2015.

[39] Zhi Peng Li, Toshiyuki Mori, Graeme John Auchterlonie, Jin Zou, and John Drennan. Two types of diffusions at the cathode/electrolyte interface in IT-SOFCs. *Journal of Solid State Chemistry*, 184(9):2458–2461, 2011.

[40] S. S. Shy, C. M. Huang, H. H. Li, and C. H. Lee. The impact of flow distributors on the performance of solid oxide fuel cell - Part II: Electrochemical impedance measurements. *Journal of Power Sources*, 196(18):7555–7563, 2011.

[41] John T S Irvine, Derek C. Sinclair, and Anthony R. West. Electroceramics: Characterization by Impedance Spectroscopy. *Advanced Materials*, 2(3):132–138, 1990.

[42] James Larminie and Andrew Dicks. *Fuel Cell Systems Explained*. Wiley, 2nd edition, 2003.

[43] Frank S Baumann, Jürgen Fleig, Hanns-ulrich Habermeier, and Joachim Maier. Impedance Spectroscopic study on well-defined (La,Sr)(Co,Fe)O3-δ model electrodes. *Solid State Ionics*, pages 1071–1081, 2006.

[44] Bruker TOPAS software. https://www.bruker.com/products/x-ray-diffraction-and-elemental-analysis/x-ray-diffraction/xrd-software/topas.html. Accessed: 23.05.2017, 2017.

[45] Bruker Eva software. https://www.bruker.com/products/x-ray-diffraction-and-elemental-analysis/x-ray-diffraction/xrd-software/eva/overview.html. Accessed: 16.10.2016.

[46] ZView software. http://www.scribner.com/software/general-electrochemistry/68-general-electrochemistr/376-zview-for-windows. Accessed: 23.04.2017.

[47] Joseph Goldstein. *Scanning Electron Microscopy and X-Ray Microanalysis*. Kluwer Academic/Plenum Publishers, 3rd edition, 2003.

[48] S. J. Skinner. Recent advances in Perovskite-type materials for solid oxide fuel cell cathodes. *International Journal of Inorganic Materials*, 3(2):113–121, 2001.

[49] V. V. Kharton, Fm Figueiredo, L Navarro, En Naumovich, Av Kovalevsky, Aa Yaremchenko, Ap Viskup, a Carneiro, Fmb Marques, and Jr Frade. Ceria-based materials for solid oxide fuel cells. *Journal of Materials Science*, 36(5):1105–1117, 2001.

[50] Azad J. Darbandi and Horst Hahn. Nanoparticulate cathode thin films with high electrochemical activity for low temperature SOFC applications. *Solid State Ionics*, 180(26-27):1379–1387, 2009.

[51] Jimmi Nielsen, Torben Jacobsen, and Marie Wandel. Impedance of porous IT-SOFC LSCF:CGO composite cathodes. *Electrochimica Acta*, 56(23):7963–7974, 2011.

[52] Jaroslaw Sar, Laurent Dessemond, and Elisabeth Djurado. Electrochemical properties of graded and intermediate-temperature solid oxide fuel cells. *International Journal of Hydrogen Energy*, 41(38):17037–17043, 2016.

[53] Hiroyuki Shimada, Toshiaki Yamaguchi, Toshio Suzuki, Hirofumi Sumi, Koichi Hamamoto, and Yoshinobu Fujishiro. High power density cell using nanostructured Sr-doped SmCoO3 and Sm-doped CeO2 composite pow-

der synthesized by spray pyrolysis. *Journal of Power Sources*, 302:308–314, 2016.

[54] A. Heel, P. Holtappels, P. Hug, and T. Graule. Flame Spray Synthesis of Nanoscale La0.6Sr0.4Co0.2Fe0.8O(3-δ) and Ba0.5Sr0.5Co0.8Fe0.2O(3-δ) as Cathode Materials for Intermediate Temperature Solid Oxide Fuel Cells. *Fuel Cells*, 10(3):419–432, 2010.

[55] K. Dumaisnil, D. Fasquelle, M. Mascot, a. Rolle, P. Roussel, S. Minaud, B. Duponchel, R.-N. Vannier, and J.-C. Carru. Synthesis and characterization of La0.6Sr0.4Co0.8Fe0.2O3 films for solid oxide fuel cell cathodes. *Thin Solid Films*, 553(3):89–92, 2014.

[56] J. Zhou, G. Chen, K. Wu, and Y. Cheng. La0.8Sr1.2CoO4-CGO composite as cathode on La0.9Sr0.1Ga0.8Mg0.2O3 electrolyte for intermediate temperature solid oxide fuel cells. *Journal of Power Sources*, 232:332–337, 2013.

[57] T Tsai. Effect of LSM-YSZ cathode on thin-electrolyte solid oxide fuel cell performance. *Solid State Ionics*, 93(3-4):207–217, 1997.

[58] M. V. Anan'ev, E. Kh. Kurumchin, G. K. Vdovin, and N. M. Bershitskaya. Kinetics of Interaction of Gas Phase Oxygen with Cerium-Gadolinium Oxide. *Russian Journal of Electrochemistry*, 48(9):871–878, 2012.

[59] B.C.H. Steele and Joong-Myeon Bae. Properties of La0.6Sr0.4Co0.2Fe0.8O(3-δ) (LSCF) double layer cathodes on gadolinium-doped cerium oxide (CGO) electrolytes II. Role of oxygen exchange and diffusion. *Solid State Ionics*, 106:255–261, 1998.

[60] E. N. Armstrong, K. L. Duncan, D. J. Oh, J. F. Weaver, and E. D. Wachsman. Determination of Surface Exchange Coefficients of LSM, LSCF, YSZ, GDC Constituent Materials in Composite SOFC Cathodes. *Journal of The Electrochemical Society*, 158(5):492, 2011.

[61] Cahit Benel, Horst Hahn, and Wolfgang Ensinger. *Nanostructured Electrodes for Low Temperature Solid Oxide Fuel Cells*. PhD thesis, 2016.

[62] Xing Fan, Chun Yan You, Ji Liang Zhu, Lu Chen, and Chang Rong Xia. Fabrication of LSM-SDC composite cathodes for intermediate-temperature solid oxide fuel cells. *Ionics*, 21(8):2253–2258, 2015.

[63] A. Esquirol, N. P. Brandon, J. A. Kilner, and M. Mogensen. Electrochemical Characterization of La0.6Sr0.4Co0.2Fe0.8O3-Cathodes for Intermediate-Temperature SOFCs. *Journal of The Electrochemical Society*, 151(11):1847, 2004.

[64] C. M. Chanquía, L. Mogni, H.E. Troiani, and A. Caneiro. Highly active La0.4Sr0.6Co0.8Fe 0.2O3-x nanocatalyst for oxygen reduction in intermediate temperature-solid oxide fuel cells. *Journal of Power Sources*, 270:457–467, 2014.

Appendix A

Crystallite size of tested cathodes

Fig. A.1 and Fig. A.2 show the diffractograms of Composite A and Composite B cathode, respectively, heat treated at 950 °C and 1050 °C.

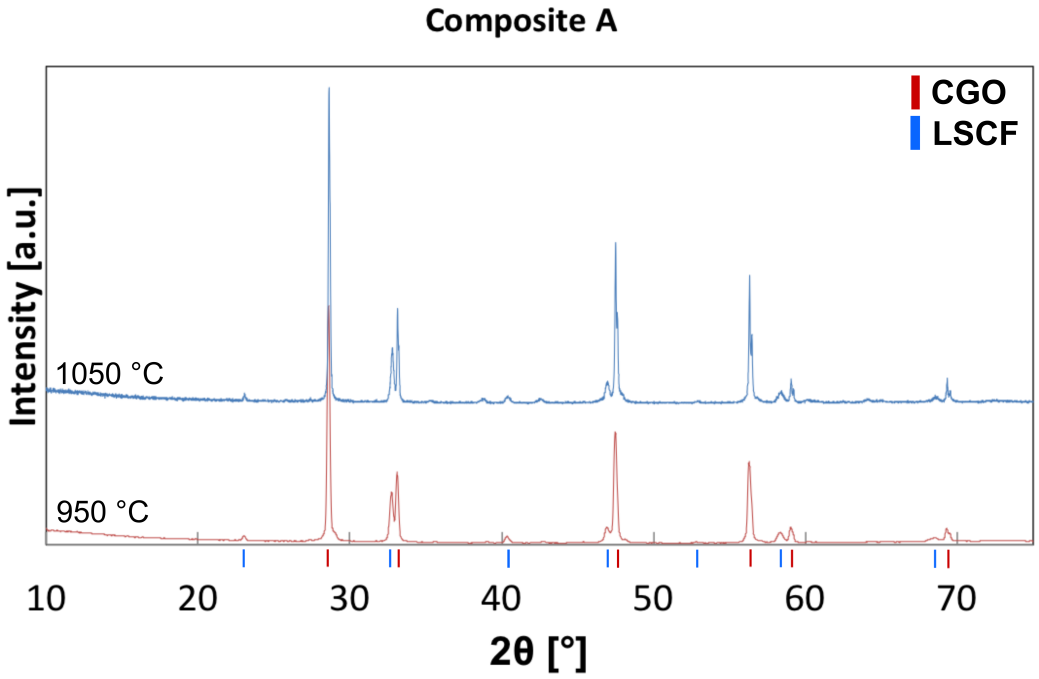

Figure A.1: Diffractograms of Composite A cathode, heat treated at 950 °C and 1050 °C.

The crystallite size of LSCF and CGO as a function of heat treatment temperature is plotted in Fig. A.3. The values at temperature 600 °C, 700 °C and 800 °C are obtained during previous work [1].

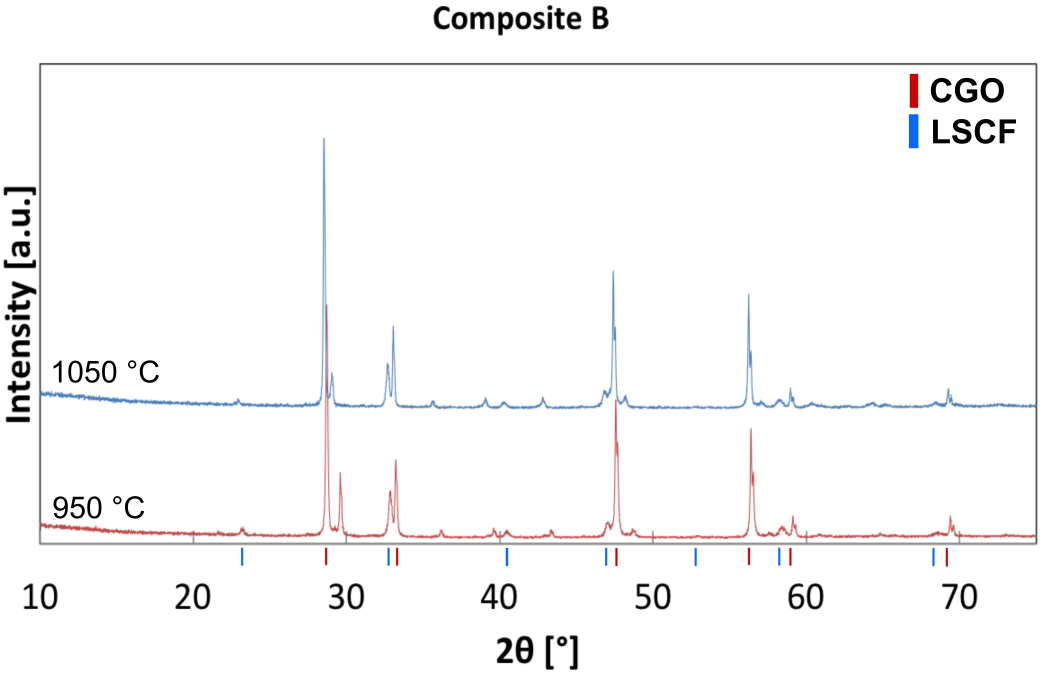

Figure A.2: Diffractograms of Composite B cathode, heat treated at 950 °C and 1050 °C.

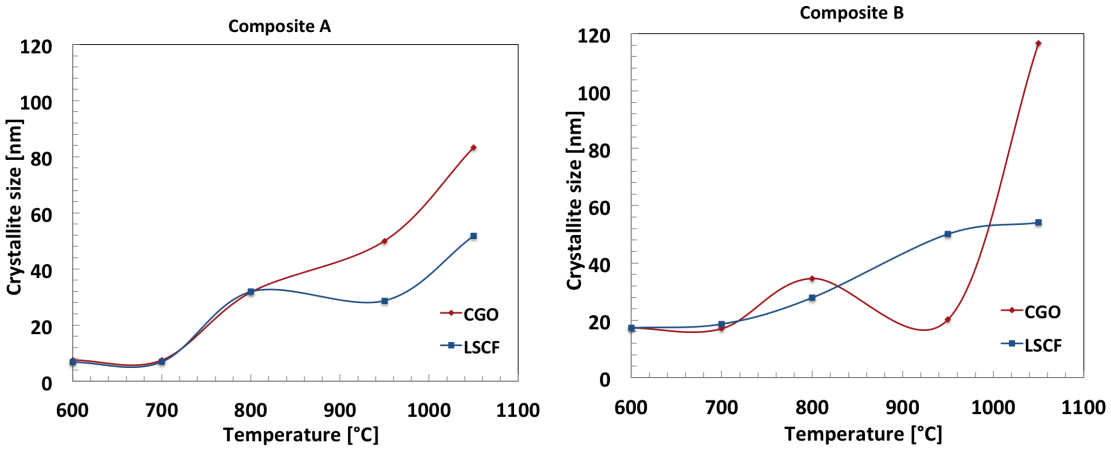

Figure A.3: Crystallite size for LSCF and CGO in (a) Composite A and (b) Composite B as a function of heat treatment temperature. The results obtained for 600 °C, 700 °C and 800 °C is obtained i previous work [1]. Calculations are done in Topas software.

Appendix B

Density calculations

B.1 Pre-study samples

The density of the samples investigated in the pre-study was calculated, and can be seen in Tab. B.1, based on the thickness of the cathodes found during SEM-analysis, the mass deposited and the theoretical density of the composite material.

Table B.1: Calculated density of samples investigated in the pre-study. The density is divided by the theoretical density of the composite cathode. The area is calculated from the radius of the samples.

Sample	**Area [cm^2]**	**Thickness [cm]**	**Volume [cm^3]**	**Mass [g]**	**Density [g/cm^3]**	**Theoretical density [g/cm^3]**	**Density %**
A850	1.122	0.000244	0.000274	0.0005	1.826	7.274	25.1
A950	1.110	0.000734	0.000815	0.0021	2.578	7.274	35.4
A1050	1.121	0.000619	0.000694	0.0021	3.026	7.274	41.6
A1150	1.120	0.000580	0.000650	0.0021	3.233	7.274	44.4
B850	1.120	0.000246	0.000276	0.0005	1.815	7.274	24.9
B950	1.112	0.000501	0.000557	0.0021	3.769	7.274	51.8
B1050	1.110	0.000429	0.000476	0.0021	4.410	7.274	60.6
B1150	1.112	0.000318	0.000354	0.0021	5.938	7.274	81.6

B.2 Tested samples

The density of the samples investigated in the pre-study was calculated, and can be seen in Tab. B.1, based on the thickness of the cathodes found during SEM-analysis, the mass deposited and the theoretical density of the composite material.

Table B.2: Density of tested samples. The density is divided by the theoretical density of the composite cathode. The area is calculated from the radius of the samples.

Sample	**Area [cm^2]**	**Thickness [cm]**	**Volume [cm^3]**	**Mass [g]**	**Density [g/cm^3]**	**Theoretical density [g/cm^3]**	**Density %**
A950	1.122	0.00109	0.00122	0.0025	2.045	7.274	28.1
A1050	1.108	0.00062	0.00069	0.0024	3.468	7.274	47.7
B950	1.110	0.00056	0.00062	0.0021	3.377	7.274	46.4
B1050	1.169	0.00050	0.00058	0.0027	4.634	7.274	63.7

Appendix C

Nyquist-plots, raw data

C.1 Example of noisy data

In Fig. C.1, an example of raw data with noise is presented. The data is from impedance measurements of A1050 at operating temperature 800 °C.

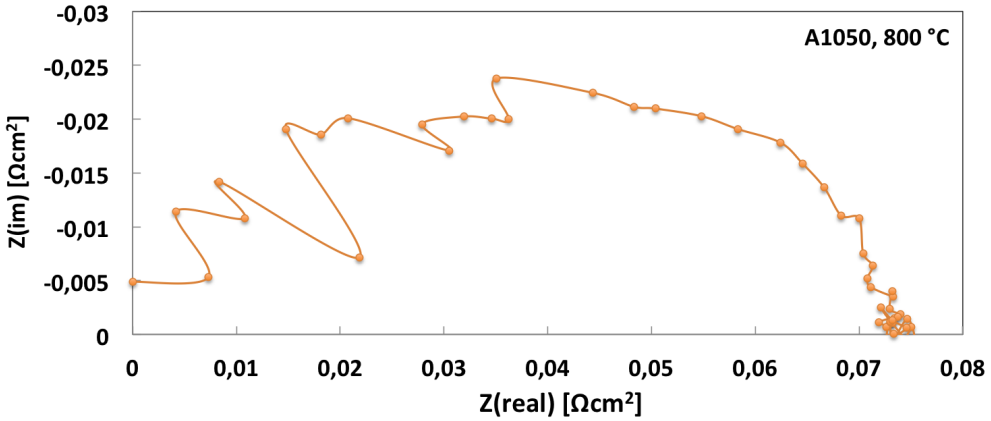

Figure C.1: Nyquist-plot, obtained from A1050 at 800 °C. The plot is normalized.

C.2 Raw data Nyquist-plot with fitted curve

In Fig. C.2, example of a fitted curve can be seen. This is form impedance measurements of A1050 at operating temperature 600 °.

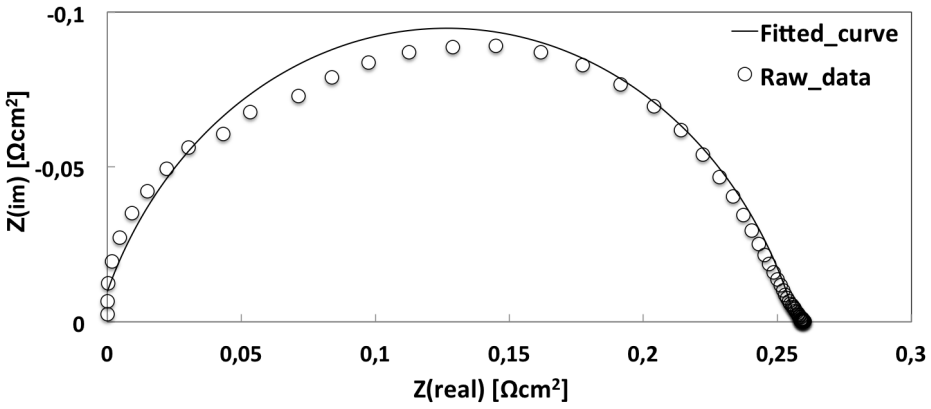

Figure C.2: Nyquist-plot, the raw-data and fitted curve of A1050 at 600 °C.